IEEE ComSoc
IEEE Open Journal of the
Communications Society

On Performance of Integrated Satellite HAPS Ground Communication: Aerial IRS Node vs Terrestrial IRS Node

Parvez Shaik[1], Kamal Kishore Garg [2], Praveen Kumar Singya [3], Vimal Bhatia[4], SENIOR MEMBER, IEEE, Ondrej Krejcar[5], AND Mohamed-Slim Alouini.[6], FELLOW, IEEE

[1]Electrical and Computer Engineering Program, Texas A&M University at Qatar, Doha, Qatar
[2]School of Technology, Pandit Deendayal Energy University, Gandhinagar, Gujarat, India
[3] Department of Electrical and Electronics Engineering, ABV-IIITM Gwalior, India
[4]Department of Electrical Engineering, Indian Institute of Technology Indore, Indore-453552, India
[5]Faculty of Informatics and Management, University of Hradec Kralove, 50003 Hradec Kralove, Czech Republic
[6]Computer, Electrical, and Mathematical Science and Engineering (CEMSE) Division, King Abdullah University of Science and Technology (KAUST), Thuwal 23955-6900, Saudi Arabia

CORRESPONDING AUTHOR:Parvez Shaik (e-mail: parvez.shaik@qatar.tamu.edu).

ABSTRACT With an objective of ubiquitous connectivity around the world with enhanced spectral efficiency, intelligent reflecting surfaces (IRS) integrated satellite-terrestrial communications is a topic of research interest specially in infrastructure-deficient terrains. In line with this vision, this paper entails the performance analysis of satellite-terrestrial networks leveraging both aerial and terrestrial IRS nodes, with the support of high altitude platforms (HAPS) over diverse fading channels including shadowed Rician, Rician, and Nakagami-m fading channels. The merits of IRS in enhancing spectral efficiency is analyzed through closed-form expressions of outage probability and ergodic rate. Further, the average symbol error rate analysis for the higher-order quadrature amplitude modulation (QAM) schemes such as hexagonal QAM, rectangular QAM, cross QAM, and square QAM is performed. Practical constraints like antenna gains, path loss, and link fading are considered to characterize the satellite terrestrial links. Finally, a comparison between the HAPs based IRS node and terrestrial IRS nodes is performed and various insights are drawn under various fading scenarios and path loss conditions. Our results demonstrate that aerial IRS nodes offer superior performance in terms of outage probability, ergodic rate, and symbol error rate for higher-order QAM schemes. Additionally, the study reveals that the ergodic rate in aerial IRS systems scales with the number of IRS elements, while terrestrial IRS systems rely on the diversity of the satellite-HAP link.

INDEX TERMS IRS, HAP, Nakagami-m, Rician, shadowed Rician, ergodic rate, HQAM, RQAM, XQAM.

I. Introduction

DRIVEN by the desire for unprecedented seamless connectivity and ultra-low latency, the research community is rapidly advancing towards 6G communications. However, the current terrestrial networks poses fundamental challenges in achieving the ambitious 6G KPIs [1]. Existing TN infrastructure is vulnerable to natural disasters and network densification inevitably causing serious economic and environmental concerns as well as energy crunch [2]. To circumvent these limitations, in the blueprint of beyond 5G and 6G future telecommunications, the non-terrestrial networks (NTNs) play an important role in achieving the ambitious KPIs which were not fulfilled by the TN alone [3].

With the recent technological advancement and evolution, 3GPP has embraced this potential vision and detailed it in technical reports [4].

In general, the NTNs are satellites, HAPs, and UAVs which are distinguished based on the height, frequency, coverage area, and propagation of flight operation [5]. HAPs act as data center between the UAVs and the satellites. Aerial networks are capable of ensuring unmatched connectivity and services even in the remote inaccessible terrains. However, in practice, aerial networks performance is hampered due to shadowing, path losses, antenna misalignment, power constraints, and hardware limitations [6]. With the technological advances, an innovative solution in the form of IRS has

emerged which plays a crucial role in realizing the system level KPIs for TN and NTNs for 6G communications.

IRS generates an intelligent smart radio propagation environment to control the planar wavefront of the incident signal to increase the signal strength [7]. IRS is a group of planar software defined advanced microelectrical mechanical systems and metamaterials which are engineered electronically to reconfigure the wave steering to realize a desired transformation in time-varying wireless propagation environments [8]. Hence, IRS is appealing technology to integrate with the satellite-terrestrial communications to meet the 6G KPIs.

Research community in the academia and industry presented their studies on prospects of potential improvements in the wireless systems with the integration of IRS. Authors in [9] investigated the performance of IRS based satellite communications and analyzed the error rates. Xu *et al.* [10], addressed the secured cooperative communications with IRS for satellite-terrestrial links. The authors in [11] performed secrecy maximization for high mobility drone communication with IRS. To address the challenge of design and optimization of beamforming for the IRS within a NTN, the authors presented their study in [12]–[14]. To address the prospects of coverage area improvements, the authors of [15], [16] proposed satellite-IRS-user links deployments. The potential use cases and challenges associated with IRS integration with aerial platforms are presented in [5], [17]. In [18], authors studied IRS assisted non-terrestrial and inter-planetary communications, along with the performance of IRS assisted NTNs. A comparative study is presented with IRS and cooperative relays systems in [19], [20] to explore the potentiality of IRS over relays. Dolas *et.al* [21] studied satellite-terrestrial system in terms of outage probability and error rate analysis by modeling satellite to relay link with Shadowed-Rician distributed and cascaded relay-IRS-destination link is Rayleigh distributed. In [22], authors investigated an IRS-aided integrated terrestrial-satellite network system by deploying IRS to assist both the terrestrial and satellite systems. Majority of work in the literature consider IRS in the terrestrial link of NTNs considered. However, analysis of IRS in NTNs as a aerial node versus a terrestrial node is missing. It is expected that in the future IRS to be mounted as aerial nodes. Thus we attempt to address the issue by considering IRS as a aerial node and a terrestrial node for a integrated satellite HAP ground communication. A comparative study with the similar works is presented in TABLE I. In TABLE I, Sat. indicates satellite and Ter. to Terrestrial.

On the other hand, the signal characteristics especially modulation schemes play a vital role for a reliable power-efficient high-speed communications. In this prospective, the bandwidth and power efficient higher-order QAM schemes have gained significant attraction. Depending on the constellations, family of QAMs includes SQAM, RQAM, cross QAM (XQAM), and HQAM [25]. In the past, majority of

the works on the ASER of higher-order QAM schemes are performed in RF communications, OWC (especially ultra-violet communications and free space optics), and in mixed RF/OWC systems [26]–[30]. Thus it is of high interest to perform ASER analysis of higher order QAM schemes for the system employing IRS.

A. Motivation

By incorporating an Intelligent Reflecting Surface (IRS) into wireless networks, a highly probabilistic radio environment with programmable and partially deterministic space is established. In existing literature, most works predominantly examines IRS by taking similar channel models into consideration for the transmission from the transmitter to the receiver via an IRS. However, such models often fall short in fully capturing the complexity of the propagation environment. This article seeks to address this limitation by exploring a wider range of channel models to capture the complexities of real-world propagation environments. Another objective of this article is to underscore the versatility of IRS, demonstrating its potential to function effectively either as a terrestrial or aerial node within network infrastructures. In this context, the present work focuses on two distinct system models with LOS (Aerial IRS Nodes) and Non-LoS (Terrestrial IRS Nodes)

B. Contribution

Considering the above system models, the main contributions of this work are as follows:

- **Analytical framework:** We derive closed-form expressions for the end-to-end (e2e) signal-to-noise ratio (SNR) cumulative distribution function (CDF) and outage probability for both system models. This includes illustrating the impact of antenna beam, path loss, and satellite beam gains on system performance.
- **ASER analysis:** We investigate the ASER performance of different QAM schemes (HQAM, RQAM, XQAM) in both scenarios, providing valuable insights into system behavior in attaining the rates of transmission.
- **Capacity analysis:** We derive closed-form expressions for the ergodic rate of both systems, enabling the determination of their maximum achievable transmission rates. Furthermore, we demonstrate the improvement in the capacity with an increase in IRS elements under challenging channel conditions.
- **Impact of system parameters** We comprehensively analyze the influence of various parameters on system performance, including path losses (antenna beam, rain attenuation, free-space path loss), satellite beam angle, and the number of IRS elements. We also consider diverse fading channel conditions in this analysis.

Notations: Column vectors are denoted by bold lowercase letters; Squared Frobenius norm is denoted by $|| \cdot ||^2$. Nakagami-m distribution with fading severity m and vari-

TABLE 1. Comparison of the presented work with other similar works.

	[9]	[23]	[21]	[22]	[24]	This work
System Model	Satellite Communications	Terrestrial Communications	Sat.-Ter. Communications	Sat.-Ter. Communications	UAV-Ter. Communications	Sat.-Ter. Communications
Channel model	Terahertz links	Rician	Shadowed Rician Rayleigh	Shadowed Rician Rician	Rayleigh	Shadowed Rician Rician Nakagami-m
Terrestrial IRS node	✗	✓	✓	✓	✗	✓
Aerial IRS node	✗	✗	✗	✗	✓	✓
Comparative study	✗	✗	✗	✗	✗	✓
Outage analysis	✗	✓	✓	✗	✗	✓
Ergodic rate analysis	✓	✓	✓	Weighted sum rate	✗	✓
ASER Analysis {S, R, H, X}QAM	BPSK	✗	QPSK	✗	SQAM	✓

TABLE 2. List of acronyms and their descriptions.

2D	2 dimensional
6G	Sixth-generation
3GPP	Third Generation Partnership Project
AWGN	Additive white Gaussian noise
AF	Amplify-and-forward
AG	Air-to-ground
ASER	Average symbol-error-rate
AWGN	Additive white Gaussian noise
BS	Base station
BER	Bit-error-rate
BPSK	Binary phase shift keying
CDF	Cumulative distribution function
CSI	channel state information
DF	Decode-and-forward
e2e	End-to-end
FSO	Free space optics
HQAM	Hexagonal QAM
HAPs	High-altitude platforms
i.i.d.	Independent and identically distributed
IRS	Intelligent Reflecting Surfaces
ITU	International Telecommunication Union
KPIs	key Performance Indicators
LAPs	Low-altitude platforms
LBFGS	Limited-memory Broyden-Fletcher-Goldfarb-Shanno
LoS	Line-of-sight
MIMO	Multiple-input and multiple-output
MMSE	Minimum mean square error
MOP	Minimum outage probability
NTNs	Non-Terrestrial Networks
OWC	Optical wireless communication
PDF	Probability density function
QAM	Quadrature amplitude modulation
QoS	Quality-of-service
QPSK	Quadrature phase shift keying
RF	Radio frequency
RQAM	Rectangular QAM
SQAM	Square QAM
SER	Symbol-error-rate
SEP	Symbol-error-probability
SIR	Signal-to-interference-ratio
SNR	Signal-to-noise ratio
TN	Terrestrial Network
UAVs	Unmanned aerial vehicles
UVC	Ultraviolet communication
UEs	User Equipments
XQAM	Cross QAM

ance σ_m^2 is denoted by $\text{Nak}(m, \sigma_m^2)$. Complex Gaussian distribution with mean 0, variance σ^2 is denoted by $\mathcal{CN}(0, \sigma^2)$. Confluent Hypergeometric function (HF) of first kind and Gauss HF are represented by $_1F_1(a, b, c)$ and $_2F_1(a, b, c, d)$, respectively. Probability density function (PDF) and cumulative distribution function (CDF) are given by $f(\cdot)$ and $F(\cdot)$, respectively. Generalized Marcum Q-function is given by $Q_m(\cdot, \cdot)$. Statistical expectation operator and variance are denoted by $\text{E}\{(\cdot)\}$ and $\text{Var}\{(\cdot)\}$, respectively. Modified Bessel function of first kind with order ϑ is denoted as $I_\vartheta(\cdot)$. Bessel function of first kind with order ϱ is denoted as $J_\varrho(\cdot)$. Exponential integral function is denoted as $\mathbf{Ei}(\cdot)$. Gamma function is represented by $\Gamma(\cdot)$. Upper incomplete gamma function with parameters {a,b} is represented as $\Gamma(a, b)$. Finally, $G_{p,q}^{m,n}\left(\begin{array}{c} a_1, a_2, ..., a_p \\ b_1, b_2, ..., b_q \end{array}\middle| z\right)$ is the Meijer-G function with $0 \le m \le q$ and $0 \le n \le p$, where m, n, p, and q are integers.

II. System Modeling

In this Section, the system models considered are presented and discussed.

- System Model 1 (LoS): This model involves three nodes: a satellite (S) as the information source, an IRS mounted on a High-Altitude Platform (HAP) with N-elements (H_I), and an end user (U) as the destination node. The channel link S → H_I exhibits dominant LoS propagation, modeled by Rician fading. The link H_I → U is modeled using SR fading to capture the impact of NTN-TN links. This is referred to as SM-1 in the paper.

- System Model 2 (Non-LoS (NLoS)): The possibility existence of proper LoS propagation from satellite to IRS directly may not be feasible due to the large distance, non-static stratospheric winds, or stratospheric attenuation [31]–[35]. Hence, we have considered HAP as a relay between the satellite to TNs. This model

involves four nodes: a satellite (S) as the information source, a HAP acting as a decode-and-forward (DF) relay (H_R), a terrestrial IRS with N-elements (I_N), and an end user (U) as the destination node. The S $\rightarrow$ H_R link assumes an LoS path modeled by Rician fading (hs). The link HI $\rightarrow$ I_N is modeled with SR fading (h_i), while the terrestrial link $I_N \rightarrow$ U is modeled using generalized Nakagami-m flat fading channels. This configuration is designed to handle NLoS scenarios effectively by employing a terrestrial relay node with IRS deployment to forward data from the HAP to terrestrial users. This is referred to as SM-2 in the paper.

For both system models, it is assumed that a communication-oriented software ensures precise control of phase-shifts for incident signals on the IRS, enabling coherent/constructive signal combining at the end user (U) to maximize the e2e signal-to-noise ratio (SNR). This coherent combining technique enhances the overall system performance.

III. Statistical characterization of Channel

A. Channel Modeling

This section focuses on the statistical properties and the channel models of both the satellite and the terrestrial links, present in the considered system models. For the design and performance analysis of the real-time operation based satellite-terrestrial mobile communications, shadowed Rician (SR) model is employed to model both narrowband and wideband communications [36].
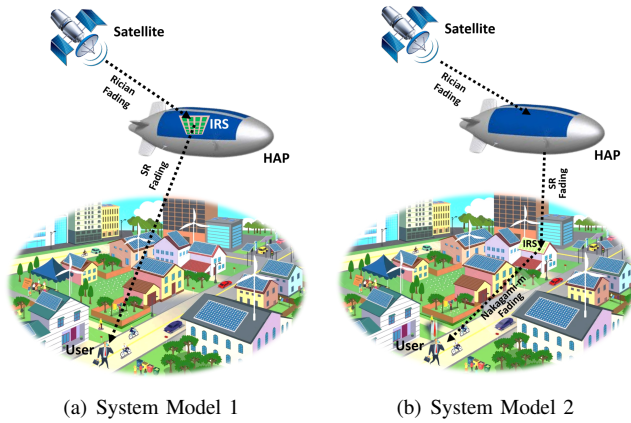

(a) System Model 1   (b) System Model 2

FIGURE 1. Integrated satellite HAPs ground communication system models

The statistical characterization of the channels is as follows:

1) Rician Fading Channel

The channel gain γ is noncentral-χ^2 distributed and the probability density function (PDF) of the Rician fading channel is given as [37],

$$f_{\gamma_i}(\gamma) = \frac{(K+1)e^{-K}}{\bar{\gamma}_i} e^{\frac{-(K+1)\gamma}{\bar{\gamma}_i}}$$
$$\times I_0\left(2\sqrt{\frac{K(K+1)\gamma}{\bar{\gamma}_i}}\right), \quad \gamma \geq 0 \qquad (1)$$

where K is the Rician K-factor, $\bar{\gamma}_i = \frac{\Omega_i}{\sigma_N^2}$, Ω_i is the average fading power of the ith link, and σ_N^2 is the power of the AWGN component. The CDF is given as [38],

$$F_{\gamma_i}(\gamma) = 1 - \mathcal{Q}_1\left(\sqrt{(2K)}, \sqrt{\frac{2(K+1)\gamma}{\bar{\gamma}_i}}\right), \quad \gamma \geq 0 \quad (2)$$

where $S_R = \mu_R$ and local-mean scattered power is given as $\sigma_R^2 = \sqrt{\frac{S_R^2}{2K}}$. The kth moment of the Rician fading channels is given as $\mathrm{E}[x^k] = \left(2\sigma_R^2\right)^{\frac{k}{2}} \Gamma\left(1 + \frac{k}{2}\right) {}_1F_1\left(-\frac{k}{2}, 1, -K\right)$.

2) Shadowed Rician Fading Channel

The components of SR fading channels are considered to be independent and identically distributed as $g_i = Z\exp(j\zeta) + A\exp(j\psi)$ [36], where independent stationary random processes Z and A are the amplitudes of the LoS and the scatter components, which follow Nakagami-m and Rayleigh distributions, respectively. In addition, ζ is the deterministic phase of the LoS component, while ψ is the stationary random phase process with uniform distribution over $[0, 2\pi)$, which are independent of Z and A. The shadowed Rician fading channel PDF of $|g_i|^2$ is given as [36],

$$f_{|g_i|^2} = \alpha e^{-\beta x} {}_1F_1\left(m; 1; \delta x\right), \quad x \geq 0 \qquad (3)$$

where $\alpha = \frac{\left[\frac{2bm}{2bm+\Omega}\right]^m}{2b}$, $\beta = \frac{1}{2b}$, and $\delta = \frac{\Omega}{2b[2bm+\Omega]}$, Ω is the average power of the LoS component (Z) given by $\Omega = \mathrm{E}[Z^2]$. Also, the average power of the scatter component is given by $2b = \mathrm{E}[A^2]$, $m = \frac{(\mathrm{E}[Z^2])^2}{\mathrm{Var}[Z^2]}$, Nakagami-$m$ parameter corresponding to severity of fading, and Rician parameter $K = \frac{\Omega}{2b}$. For different types of shadowing, the values of (b, m, Ω) are given in [36, Table III]. The kth moment of the shadowed Rician fading channels is given as [36]

$$\mathrm{E}[x^k] = \left(\frac{2b_0 m}{2b_0 m + \Omega}\right)^m (2b_0)^{k/2} \Gamma\left(\frac{k}{2} + 1\right)$$
$$\times {}_2F_1\left(\frac{k}{2} + 1, m, 1, \frac{\Omega}{2b_0 m + \Omega}\right)$$
$$k = 0, 1, 2, \ldots \qquad (4)$$

The closed-form PDF expression of $||\mathbf{g}_i||^2 = \sum_{i=1}^{N} |g_i|^2$ is given as [3, eq. 26]

$$f_{||g_i||^2} = \frac{\alpha}{\Gamma(N)} x^{N-1} e^{-\beta x} {}_1F_1\left(Nm; N; \delta x\right), \quad x \geq 0 \quad (5)$$

3) Nakagami-m fading channel

The PDF of the Nakagami-m flat fading channel is given as [38]

$$f_{g_i}(x) = \frac{2x^{2m_g-1}}{\Gamma(m_g)\zeta_g^{m_g}} \exp\left(\frac{-x^2}{\zeta_g}\right), \quad x \geq 0 \qquad (6)$$

where $\zeta_g = \frac{\sigma_g^2}{m_g}$. The kth moment of the Nakagami-m fading channels is given as $\mathrm{E}[x^k] = \frac{\Gamma(m+\frac{k}{2})}{\Gamma(m)} \left(\frac{\sigma^2}{m}\right)^{\frac{k}{2}}$ [38],

4) Pathloss Modeling

In this subsection, path losses are discussed which are essential in modeling the realistic scenarios of satellite-terrestrial communication

S → H Link

The considered path loss includes the effects of antenna beam and free path loss and is given as [39]

$$PL_{\mathrm{SH}} = \frac{\lambda_c \sqrt{G_S G_H}}{4\pi d_{\mathrm{SH}} \sqrt{K_B T_{\mathrm{N_0}} B_{\mathrm{N_0}}}}, \qquad (7)$$

where λ_c is the operating carrier wavelength, G_H is the gain of HAP, d_{SH} is the distance between the GEO stationary satellite and the HAP, K_B is the Boltzmann constant (1.38×10^{-23} joule/K), $T_{\mathrm{N_0}}$ is the system noise temperature (300 K), and $B_{\mathrm{N_0}}$ is the receiver noise bandwidth (20 MHz). Further, G_S is the satellite beam gain which is given as

$$G_S = G_{\mathrm{Max}} \left(\frac{J_1(u_H)}{2u_H} + 36\frac{J_3(u_H)}{u_H^3}\right)^2, \qquad (8)$$

where G_{Max} is the maximum satellite beam gain. Also, $u_H = 2.07123\frac{\sin(\phi_{\mathrm{SH}})}{\sin(\phi_{\mathrm{3dB}})}$ with ϕ_{SH} being the angle between H and S and ϕ_{3dB} is the 3dB satellite beam angle.

Other links:

In the system model of Figure 1(a), for the $\mathrm{H_I} \rightarrow \mathrm{U}$ link and in system model Figure 1(b), for $\mathrm{H_R} \rightarrow \mathrm{I_N}$ link, the path loss are modeled as $PL_{(\mathrm{uv})}[\mathrm{dB}] = G_{\mathrm{Tx}} + G_{\mathrm{Rx}} - L_{\mathrm{FSPL}} - L_{\mathrm{Rain}} - L_{\mathrm{Atm.}} - L_{\mathrm{oth}}$, where $\{uv\} \in \{\mathrm{H_IU}, \mathrm{H_RI_N}\}$, G_{Tx} is the transmitter antenna gain (in dB), G_{Rx} is the receiver antenna gain (in dB), L_{Rain} is the rain induced loss (in dB/km), $L_{\mathrm{Atm.}}$ is the gaseous atmospheric absorption loss, L_{oth} are other miscellaneous losses (in dB). Further, L_{FSPL} is the free-space path loss (in dB), given as $L_{\mathrm{FSPL}} = 92.45 + 20\log_{10}(f_c) + 20\log_{10}(d_{\mathrm{uv}})$ with f_c being the carrier frequency, and d_{uv} is the distance between the nodes u and v.

$\mathrm{I_N} \rightarrow \mathrm{U}$ link:

In system model of Figure 1(b), the path loss corresponding to the $\mathrm{I_N} \rightarrow \mathrm{U}$ link is modeled as: $PL_{(\mathrm{I_N} \rightarrow \mathrm{U})}[\mathrm{dB}] = 40\log_{10}(d_{\mathrm{I_N U}}) - 10\log_{10}(Gt_{\mathrm{IRS}}) -$

$10\log_{10}(Gr_{\mathrm{U}}) - 20\log_{10}(h_t) - 20\log_{10}(h_r)$, where $d_{\mathrm{I_N U}}$ is the distance between $\mathrm{I_N}$ and U, Gt_{IRS} is the gain induced by IRS network, Gr_{U} is the gain of U, h_t is the height of the building upon which IRS is mounted, and h_r is the height at which the UE is situated.

IV. Performance of System Model 1

For the analysis, the channels are block-faded, where within the coherence interval, the channels are considered to be static and frequency flat. S $\rightarrow$ $\mathrm{H_I}$ link is represented as h_i whereas the $\mathrm{H_I} \rightarrow \mathrm{U}$ link is represented as g_i. Further, $0 < i \leq N$ indicates indices of the IRS element. As considered, when a signal is incident on the IRS, the phase-shifts of the incident signals are controlled perfectly, whereas the signals reflected from the IRS surface are attenuated as per the reflective coefficient. Hence, S $\rightarrow$ $\mathrm{H_I}$ $\rightarrow$ U channel links for the ith IRS element is given in the polar form as

$$h_i = \alpha_i e^{j\theta}, \quad g_i = \beta_i e^{j\phi}, \qquad (9)$$

where $\alpha_i = |h_i|$ and $\beta_i = |g_i|$ are the channel amplitudes, respectively, and θ_i and ϕ_i are the phases. The PDF of $|\alpha_i|^2$ and $|\beta_i|^2$ are given in [36]. In the analysis, perfect knowledge of the channel phases of h_i and g_i for $i = 1, 2, ..., N$ at the IRS is assumed, which corresponds to the best scenario in terms of system operation and yields a performance benchmark for practical applications. The signal received at the destination is given as

$$y = \sqrt{P_t}\mathbf{g}^T \xi \mathbf{h} x + n, \qquad (10)$$

where P_t is the transmit power, $\mathbf{h}$ and $\mathbf{g}$ are the channel vectors given as $\mathbf{h} = [h_1, h_2, ..., h_N]^T$ $\mathbf{g} = [g_1, g_2, ..., g_N]^T$, respectively. Further, $\xi = \mathrm{diag}[|\kappa_1|e^{-j\Phi_1}, |\kappa_2|e^{-j\Phi_2}, ..., |\kappa_N|e^{-j\Phi_N}]$ is a matrix of IRS meta-surface induced complex valued reflection coefficient with attenuation coefficient $\kappa \in [0,1]$ and phase shift $\Phi \in [0, 2\pi]$. Also, x is the symbol transmitted with $\mathrm{E}[|x|^2] = 1$, and n is the AWGN with zero mean and σ_N^2 variance at U. The received signal at U can thus be written as

$$y = \sqrt{P_t}\left[\sum_{i=1}^{N} h_i \kappa_i e^{-j\Phi_i} g_i\right] x + n$$

$$= \sqrt{P_t}\left[\sum_{i=1}^{N} \alpha_i \beta_i \kappa_i e^{-j(\Phi_i - \theta_i - \phi_i)}\right] x + n, \qquad (11)$$

Hence, the SNR at U is obtained as

$$\gamma = \bar{\gamma}\left|\sum_{i=1}^{N} \alpha_i \beta_i \kappa_i e^{-j(\Phi_i - \theta_i - \phi_i)}\right|^2, \qquad (12)$$

where the average SNR is $\bar{\gamma} = \frac{P_t}{\sigma_N^2}$. To maximize the SNR at U, reflection coefficient induced by $\mathrm{H_I}$ is chosen optimally such that constructive interference arises and hence, $\kappa_i = 1 \forall i$ and $\Phi_i = \theta_i + \phi_i \forall i$ [40]. The optimal maximized SNR at U

:

is given as

$$\gamma = \bar{\gamma}\left|\sum_{i=1}^{N} \alpha_i \beta_i\right|^2. \qquad (13)$$

Performance Metrics:

1) Outage Probability

A system is in outage if the instantaneous SNR (γ) of the e2e link falls bellow a threshold SNR (γ_{th}). For conventionally large number of IRS elements, the outage probability can be expressed as

$$P_{out} = \Pr(\gamma < \gamma_{th}). \qquad (14)$$

Lemma 1. For sufficiently large number of IRS elements, the CDF of e2e link is given as

$$F_{\gamma_{e2e_1}}(\gamma) = 1 - Q_{\frac{1}{2}}\left(\frac{\mu_\gamma}{\sigma_\gamma}, \frac{\sqrt{\gamma}}{\sqrt{\bar{\gamma}}\sigma_\gamma}\right), \quad \gamma > 0 \qquad (15)$$

Proof:
Given in Appendix A. ∎

2) ASER Analysis

In this subsection, ASER analysis of the SM-1 for various modulation schemes is performed. The generalized ASER expression for a digital modulation scheme by using the CDF approach [26] is given as

$$P_s(e) = -\int_0^\infty P_s'(e|\gamma) F_{\Lambda_{e2e}}(\gamma) d\gamma, \qquad (16)$$

Hexagonal QAM

For M-ary HQAM scheme the conditional SEP expression over the AWGN channel is defined as [29], [41]

$$P_s(e|\gamma) = H_a Q(\sqrt{\alpha_h \gamma}) + \frac{2}{3} H_c Q^2\left(\sqrt{\frac{2\alpha_h \gamma}{3}}\right) - 2H_b$$
$$\times Q(\sqrt{\alpha_h \gamma}) Q\left(\sqrt{\frac{\alpha_h \gamma}{3}}\right), \qquad (17)$$

where the parameters H_a, H_b, and α_h for irregular HQAM are defined in [25].

Lemma 2. The generalized ASER expression for HQAM is given as

$$P_{s_1}{}^H \approx \frac{H_a}{2} - \frac{2H_b}{3} - \frac{H_b}{3\pi}{}_2F_1\left(1,1,\frac{3}{2},\frac{1}{2}\right) + \frac{\sqrt{3}H_b}{4\pi}$$
$$\times \left({}_2F_1\left(1,1,\frac{3}{2},\frac{1}{2}\right) + {}_2F_1\left(1,1,\frac{3}{2},\frac{1}{4}\right)\right) + A_2\Bigg(\alpha^\nu$$
$$\times \left(\frac{\Gamma(\mu+\nu)}{\mu}\left(\frac{1}{2}\sqrt{\frac{\alpha_h}{2\pi}}(H_b - H_a)\mathbb{F}_2(\mu,\alpha,\beta_1)\right.\right.$$
$$- \frac{H_b}{3}\sqrt{\frac{\alpha_h}{3\pi}}\mathbb{F}_2(\mu,\alpha,\beta_2) + \frac{H_b}{2}\sqrt{\frac{\alpha_h}{6\pi}}\mathbb{F}_2(\mu,\alpha,\beta_3)\right)$$
$$+ \sum_n \frac{\Gamma(\mu_2+\nu)}{\mu_2}\mathbb{F}_2(\mu_2,\alpha,\beta_4)\left(\frac{2H_b\alpha_h}{9\pi}\left(\frac{\alpha_h}{3}\right)^n\right.$$
$$\left.\left.\left.- \frac{H_b\alpha_h}{2\sqrt{3}\pi}\left\{\left(\frac{\alpha_h}{2}\right)^n + \left(\frac{\alpha_h}{6}\right)^n\right\}\right)\right)\right), \qquad (18)$$

wherein $A_2 = \sum_{k_1=0}^\infty e^{-\alpha_1^2/2} \frac{1}{k_1!}\left(\frac{\alpha_1^2}{2}\right)^{k_1} \frac{1}{\Gamma(\frac{1}{2}+k_1)}$, $\nu = \frac{1}{2} + k_1$, $\alpha = \frac{1}{2\bar{\gamma}_u \sigma_{\gamma_u}^2}$, $\mu = \frac{1}{2}$, $\beta_1 = \frac{\alpha_h}{2}$, $\beta_2 = \frac{\alpha_h}{3}$, $\beta_3 = \frac{\alpha_h}{6}$, $\mu_2 = n+1$, and $\beta_4 = \frac{2\alpha_h}{3}$.

Proof:
Given in Appendix B. ∎

Rectangular QAM

Over the AWGN channel, the conditional SEP of RQAM scheme is given as [42, eq. (14)]

$$P_s{}^R(e|\gamma) = 2\Big[R_1 Q(a_r\sqrt{\gamma}) + R_2 Q(b_r\sqrt{\gamma})$$
$$- 2R_1 R_2 Q(a_r\sqrt{\gamma}) Q(b_r\sqrt{\gamma})\Big], \qquad (19)$$

where $R_1 = 1 - \frac{1}{M_I}$, $R_2 = 1 - \frac{1}{M_Q}$, $a_r = \sqrt{\frac{6}{(M_I{}^2-1)+(M_Q^2-1)d_r{}^2}}$ and $b_r = d_r a_r$, wherein M_I and M_Q are the number of in-phase and quadrature-phase constellation points, respectively. Also, $d_r = \frac{d_Q}{d_I}$, where d_I and d_Q indicate the in-phase and quadrature decision distances, respectively.

Lemma 3. The generalized ASER expression for RQAM is given as

$$P_{s_1}{}^R \approx I_R + \frac{a_r b_r R_1 R_2}{\pi}\beta_3^{-1}\Bigg\{{}_1F_1\left(1,\frac{3}{2},\frac{B_r}{\beta_3}\right)$$
$$+ {}_1F_1\left(1,1,\frac{3}{2},\frac{A_r}{\beta_3}\right)\Bigg\} + A_2\Bigg(\alpha^\nu\Bigg(\frac{\Gamma(\mu+\nu)}{\mu}\Bigg(\frac{a_r R_1}{\sqrt{2\pi}}$$
$$\times (R_2 - 1)\mathbb{F}_2(\mu,\alpha,\beta_1) + \frac{b_r R_2(R_1 - 1)}{\sqrt{2\pi}}\mathbb{F}_2(\mu,\alpha,\beta_2)$$
$$- \sum_n \frac{a_r b_r R_1 R_2}{\pi}\frac{\Gamma(\mu_2+\nu)}{\mu_2}\mathbb{F}_2(\mu_2,\alpha,\beta_3)(B_r^n + A_r^n)\Bigg)\Bigg)\Bigg), \qquad (20)$$

where $I_R = -a_r R_1(R_2 - 1) - b_r R_2(R_1 - 1)$, $A_r = \frac{a_r{}^2}{2}$, $B_r = \frac{b_r{}^2}{2}$ $\nu = \frac{1}{2} + k_1$; $\alpha = \frac{1}{2\bar{\gamma}_u \sigma_{\gamma_u}^2}$, $\mu = \frac{1}{2}$, $\beta_1 = A_r$, $\beta_2 = B_r$, $\mu_2 = n+1$, and where $\beta_3 = \frac{(a_r{}^2 + b_r{}^2)}{2}$. SQAM is

a special case of RQAM which can be obtained by taking $M_I = M_Q = \sqrt{M}$ and $d_{IQ} = 1$.

Proof:
Given in Appendix C. ∎

Cross QAM

The conditional SEP of XQAM scheme over AWGN channel is given as [43, eq. (53)]

$$
\mathrm{P}_s{}^X(e|\gamma) = A_n Q\left(\sqrt{\frac{2\gamma}{\alpha_x}}\right) + \frac{8}{M_x N_x}\left\{\sum_l Q\left(2l\sqrt{\frac{2\gamma}{\alpha_x}}\right)\right.
$$
$$
+ Q\left(\frac{M_x - N_x}{2}\sqrt{\frac{2\gamma}{\alpha_x}}\right) - 2\sum_l Q\left(2l\sqrt{\frac{2\gamma}{\alpha_x}}\right) Q\left(\sqrt{\frac{2\gamma}{\alpha_x}}\right)
$$
$$
\left. - Q\left(\sqrt{\frac{2\gamma}{\alpha_x}}\right) Q\left(\frac{M_x - N_x}{2}\sqrt{\frac{2\gamma}{\alpha_x}}\right)\right\} + k_x Q^2\left(\sqrt{\frac{2\gamma}{\alpha_x}}\right),
$$
(21)

where $A_n = 4 - 2\frac{M_x + N_x}{M_x N_x}, \sum_l = \sum_{l=1}^{\frac{M_x - N_x}{4} - 1}$ $k_x = 4 - 4\frac{M_x + N_x}{M_x N_x} + \frac{8}{M_x N_x}$, $\alpha_x = \frac{2}{3}\left(\frac{31 M_x N_x}{32} - 1\right)$, M_x, and N_x are the number of columns and rows corresponding to RQAM.

Lemma 4. The generalized ASER expression for XQAM is given as

$$
P_{s_1}^X \approx \frac{-\mathbb{A}_X}{2} + \frac{2}{M_x N_x} + \frac{16}{M_x N_x}\sum_l \frac{l A_{x_3}^{-1}}{\pi \alpha_x}\left({}_1F_1\left(1, \frac{3}{2}, \frac{A_{x_3}^{-1}}{\alpha_x}\right)\right.
$$
$$
+ {}_1F_1\left(1, \frac{3}{2}, \frac{4l^2}{A_{x_3}\alpha_x}\right)\right) - 2\frac{A_{x_2}}{\pi \alpha_x}\beta_4^{-1}\left({}_1F_1\left(1, \frac{3}{2}, \frac{A_{x_1}^2}{\beta_4 \alpha_x}\right)\right.
$$
$$
\left. + {}_1F_1\left(1, \frac{3}{2}, \frac{1}{\beta_4 \alpha_x}\right)\right) + \frac{k_x}{\pi \alpha_x}\beta_5{}^{-1}{}_1F_1\left(1, \frac{3}{2}, \frac{1}{\beta_5 \alpha_x}\right)\right)
$$
$$
+ A_2\left(\alpha^\nu\left(\frac{\Gamma(\mu + \nu)}{\mu}\left(\frac{\mathbb{A}_X}{2\sqrt{\pi \alpha_x}}\mathbb{F}_2(\mu, \alpha, \beta_1) - \frac{A_{x_2}}{\sqrt{\pi \alpha_x}}\right.\right.\right.
$$
$$
\times \mathbb{F}_2(\mu, \alpha, \beta_2)\right) + \sum_n \frac{\Gamma(\mu_2 + \nu)}{\mu_2}\left(\frac{-16}{M_x N_x}\sum_l \frac{l}{\pi \alpha_x}\right.
$$
$$
\times \mathbb{F}_2(\mu_2, \alpha, \beta_3)\left(\left(\frac{1}{\alpha_x}\right)^n + \left(\frac{4l^2}{\alpha_x}\right)^n\right) - \frac{2A_{x_2}}{\pi \alpha_x}
$$
$$
\times \left(\left(\frac{1}{\alpha_x}\right)^n + \left(\frac{A_{x_1}^2}{\alpha_x}\right)^n\right)\mathbb{F}_2(\mu_2, \alpha, \beta_4) - \frac{k_x}{\pi \alpha_x}
$$
$$
\left.\left.\left.\times \mathbb{F}_2(\mu_2, \alpha, \beta_5)\left(\frac{1}{\alpha_x}\right)^n\right)\right)\right),
$$
(22)

where $A_{x_1} = \frac{M_x - N_x}{2}$, $A_{x_2} = \frac{M_x - N_x}{M_x N_x}$, and $A_{x_3} = \frac{4l^2 + 1}{\alpha_x}$. Further $\nu = \frac{1}{2} + k_1$, $\alpha = \frac{1}{2\bar{\gamma}_u \sigma_{\gamma_u}^2}$, $\mu_1 = \frac{1}{2}$, $\beta_1 = \frac{1}{\alpha_x}$, $\beta_2 = A_{x_1}^2\frac{1}{\alpha_x}$, $\mu_2 = n + 1$, $\beta_3 = A_{x_3}$, $\beta_4 = \frac{1 + A_{x_1}^2}{\alpha_x}$, and $\beta_5 = \frac{2}{\alpha_x}$.

Proof:
Given in Appendix D. ∎

3) Ergodic Rate Analysis

Ergodic rate is defined as the expected value of the instantaneous mutual information between the source and the receiver. It indicates the maximum rate attained by the system. The ergodic rate of the system model Figure 1(a) can be expressed as

$$
C_R = \mathrm{E}\left(\frac{1}{2}\log_2(1 + \gamma_{e2e})\right) = \mathrm{E}\left(\frac{1}{2}\log_2(1 + \gamma)\right)
$$
$$
= \frac{1}{2\ln 2}\int_0^\infty \frac{1 - F_{\gamma_{e2e}}(\gamma)}{1 + \gamma}d\gamma.
$$
(23)

Lemma 5. Ergodic rate of the considered system is given as

$$
C_{R_1} = \sum_{k_1=0}^\infty e^{-\alpha_1^2/2}\frac{1}{k_1!}\left(\frac{\alpha_1^2}{2}\right)^{k_1}\frac{1}{\Gamma(\frac{1}{2} + k_1)}\frac{1}{2\ln 2}
$$
$$
\times G_{3,1}^{2,3}\left(\frac{1}{2\bar{\gamma}\sigma_\Lambda^2}\middle| \begin{array}{c} 0, 1 \\ 0, 0, \frac{1}{2} + k_1 \end{array}\right).
$$
(24)

Proof:
Given in Appendix E. ∎

V. Performance of System Model 2

In this system model, it is assumed that the direct link between the S and U is not available due to severe blockage. S communicate with U through a DF H_R and I_N. In the first time slot, S transmit the information to H_R through an LoS path. The signal received at the H_R from S is given as

$$
y_r = \sqrt{P_s}h_s x + n_s,
$$
(25)

where P_s is the transmit power at S, x is the transmitted symbol with $\mathrm{E}[|x|^2] = 1$ and n_s is the AWGN of the S $\rightarrow H_R$ link with $n \sim \mathcal{CN}(0, \sigma^2)$. The instantaneous SNR of the S $\rightarrow H_R$ link is expressed as

$$
\gamma_s = \bar{\gamma}_s|h_s|^2
$$
(26)

where $\bar{\gamma} = \frac{P_s}{\sigma^2}$. During the second time slot, node R, decodes the signal received from the S and transmits the re-encoded symbol to the U via IRS. The signal received at U reflected by IRS is given as

$$
y_u = \sqrt{P_h}\mathbf{g_u}^T\zeta\mathbf{h_u}x + n,
$$
(27)

where P_h is the transmit power at H_R, $\mathbf{h_u}$ and $\mathbf{g_u}$ are the channel vectors corresponding to shadowed Rician fading and Nakagami-m fading and are denoted as $\mathbf{h_u} = [h_{s_1}, h_{s_2}, ..., h_{s_N}]^T$ and $\mathbf{g_u} = [g_{s_1}, g_{s_2}, ..., g_{s_N}]^T$, respectively. $\zeta = \mathrm{diag}[|\varrho_1|e^{-j\Phi_1}, |\varrho_2|e^{-j\Phi_2}, ..., |\varrho_N|e^{-j\Phi_N}]$ is a matrix of IRS meta-surface induced complex valued reflection coefficient with attenuation coefficient $\varrho \in [0, 1]$ and phase shift $\Phi \in [0, 2\pi]$. In our analysis, we assume perfect knowledge of the channel phases of h_{s_i} and g_{s_i} for $i = 1, 2, ..., N$ at the I_N, which corresponds to the best scenarios in terms of system operation and yields a performance benchmark for practical applications. The

:

received signal can be re-written as

$$y_u = \sqrt{P_h}\left[\sum_{i=1}^{N} h_{s_i}\varrho_{s_i}e^{-j\Phi_{s_i}}g_{s_i}\right]x + n$$

$$= \sqrt{P_h}\left[\sum_{i=1}^{N} \lambda_i\kappa_{s_i}\varrho_{s_i}e^{-j(\Phi_{s_i}-\theta_{s_i}-\phi_{s_i})}\right]x + n, \quad (28)$$

The SNR at U is given as

$$\gamma_u = \bar{\gamma_u}\left|\sum_{i=1}^{N}\lambda_{s_i}\kappa_{s_i}\varrho_{s_i}e^{-j(\Phi_i-\theta_{s_i}-\phi_{s_i})}\right|^2, \quad (29)$$

where $\bar{\gamma_u} = \frac{P_h}{\sigma^2}$. To maximize the SNR at U, reflection coefficient induced by I_N must be chosen optimally such that constructive interference increases and hence, $\varrho_{s_i} = 1$ $\forall i$ and $\Phi_{s_i} = \theta_{s_i} + \phi_{s_i}$ $\forall i$. The optimal maximized SNR at U is given as

$$\gamma_u = \bar{\gamma_u}\left|\sum_{i=1}^{N}\lambda_{s_i}\kappa_{s_i}\right|^2. \quad (30)$$

The e2e SNR of the S $\to$ H_R $\to$ I $\to$ U link is given as

$$\gamma_{su} = \min(\gamma_s,\gamma_u) = \min\left(\bar{\gamma}_s|h_s|^2, \bar{\gamma_u}\left|\sum_{i=1}^{N}\lambda_{s_i}\kappa_{s_i}\right|^2\right). \quad (31)$$

Performance Metrics

1) Outage Probability

The e2e outage probability of the considered system model Figure 1(b) is given as

$$P_{out} = \Pr(\min(\gamma_s,\gamma_u) \le \gamma_{th}) = F_{\gamma_{su}}(\gamma),$$
$$= 1 - (1 - F_{\gamma_s}(\gamma_{th}))(1 - F_{\gamma_u}(\gamma_{th}))$$
$$= F_{\gamma_s}(\gamma_{th}) + F_{\gamma_u}(\gamma_{th}) - F_{\gamma_s}(\gamma_{th})F_{\gamma_u}(\gamma_{th}). \quad (32)$$

Lemma 6. For sufficiently large number of IRS elements, the CDF of the e2e link is given as

$$F_{\gamma_{su}}(\gamma) = 1 - Q_{\frac{1}{2}}\left(\frac{\mu_{\gamma_u}}{\sigma_{\gamma_u}},\frac{\sqrt{\gamma}}{\sqrt{\bar{\gamma}}\sigma_{\gamma_u}}\right)Q_1\left(\frac{\mu_{\gamma_s}}{\sigma_{\gamma_s}},\frac{\gamma}{\sigma_{\gamma_s}}\right), \quad \gamma > 0 \quad (33)$$

Proof:
Given in Appendix F. ∎

2) ASER Analysis

For ASER analysis, (33) can be re-written in series form [44, eq. 18] as

$$P_{out} = 1 - A_3\exp[-\Omega\gamma_{th}]\Gamma(M_2+k_2,\beta_2^2/2)\gamma_{th}^n, \quad (34)$$

where $M_2 = \frac{1}{2}$, $\alpha_2 = \frac{\mu_{\gamma_u}}{\sigma_{\gamma_u}}$, $\beta_2 = \frac{\sqrt{\gamma_{th}}}{\sqrt{\bar{\gamma_u}}\sigma_{\gamma_u}}$, and $\Omega = \left(\frac{K+1}{\gamma_{SR}}\right)$.

Remark

The above series is terminated at l=20 and verified in Mathematica. The series k_2 is terminated at 150 and verified by both Mathematica and Matlab.

Hexagonal QAM

For SM-2, the generalized ASER expression of HQAM can be obtained in a similar manner as shown in Appendix B. Also, we apply the identities [45, eq. (3.351.3), (7.522.9), (6.455.1), (9.14.1)] to obtain the generalized ASER expression of HQAM as

$$P_{s_2}^H = \frac{H_a}{2} - \frac{2H_b}{3} - \frac{H_b}{3\pi}\,_2F_1\left(1,1,\frac{3}{2},\frac{1}{2}\right) + \frac{\sqrt{3}H_b}{4\pi}$$
$$\times\left(\,_2F_1\left(1,1,\frac{3}{2},\frac{1}{2}\right) + \,_2F_1\left(1,1,\frac{3}{2},\frac{1}{4}\right)\right)$$
$$+ A_3\Bigg(\alpha^\nu\bigg(\frac{\Gamma(\mu+\nu)}{\mu}\bigg(\frac{1}{2}\sqrt{\frac{\alpha_h}{2\pi}}(H_b - H_a)\mathbb{F}_2(\mu,\alpha,\beta_1)$$
$$- \frac{H_b}{3}\sqrt{\frac{\alpha_h}{3\pi}}\mathbb{F}_2(\mu,\alpha,\beta_2) + \frac{H_b}{2}\sqrt{\frac{\alpha_h}{6\pi}}\mathbb{F}_2(\mu,\alpha,\beta_3)\bigg)$$
$$+ \sum_i\frac{\Gamma(\mu_2+\nu)}{\mu_2}\mathbb{F}_2(\mu_2,\alpha,\beta_4)\bigg(\frac{2H_b\alpha_h}{9\pi}\Big(\frac{\alpha_h}{3}\Big)^i$$
$$- \frac{H_b\alpha_h}{2\sqrt{3}\pi}\left\{\Big(\frac{\alpha_h}{2}\Big)^i + \Big(\frac{\alpha_h}{6}\Big)^i\right\}\bigg)\bigg)\Bigg), \quad (35)$$

where $\nu = \frac{1}{2} + k_1$; $\alpha = B_{\gamma_u}$, $\mu = n + \frac{1}{2}$, $\beta_1 = \frac{\alpha_h}{2} + \Omega$, $\beta_2 = \frac{\alpha_h}{3} + \Omega$, and $\beta_3 = \frac{\alpha_h}{6} + \Omega$. Further, $\mu_2 = n + i + 1$ and $\beta_4 = \frac{2\alpha_h}{3} + \Omega$.

Rectangular QAM

For SM-2, the generalized ASER expression of RQAM can be obtained in a similar manner as shown in Appendix C. Also, we apply the identities [45, eq. (3.351.3), (7.522.9), (6.455.1), (9.14.1)] to obtain the generalized ASER expression of RQAM as

$$P_{s_2}^R = I_R + \frac{a_rb_rR_1R_2}{\pi}\beta_3^{-1}\Bigg\{\,_1F_1\left(1,\frac{3}{2},\frac{B_r}{\beta_3}\right)$$
$$+ \,_1F_1\left(1,1,\frac{3}{2},\frac{A_r}{\beta_3}\right)\Bigg\} + A_3\Bigg(\alpha^\nu\bigg(\frac{\Gamma(\mu+\nu)}{\mu}\bigg(\frac{a_rR_1}{\sqrt{2\pi}}$$
$$\times(R_2-1)\mathbb{F}_2(\mu,\alpha,\beta_1) + \frac{b_rR_2(R_1-1)}{\sqrt{2\pi}}\mathbb{F}_2(\mu_2,\alpha,\beta_2)\bigg)$$
$$- \sum_i\frac{a_rb_rR_1R_2}{\pi}\frac{\Gamma(\mu_2+\nu)}{\mu_2}\mathbb{F}_2(\mu_2,\alpha,\beta_4)\left(B_r^i+A_r^i\right)\bigg)\Bigg), \quad (36)$$

where $\nu = \frac{1}{2} + k_1$; $\alpha = \frac{1}{2\bar{\gamma_u}\sigma_{\gamma_u}^2}$, $\mu = n + \frac{1}{2}$, $\beta_1 = A_r + \Omega$, $\beta_2 = B_r + \Omega$, and $\beta_3 = \frac{(a_r^2+b_r^2)}{2}$. Further, $\mu_2 = n + i + 1$, $\beta_4 = \frac{(a_r^2+b_r^2)}{2} + \Omega$.

Cross QAM

For SM-2, the generalized ASER expression of XQAM can be obtained in a similar manner as shown in Appendix D. Also, we apply the identities [45, eq. (3.351.3), (7.522.9), (6.455.1), (9.14.1)] to obtain the generalized ASER expression of XQAM as

$$P_{s_2}^X = \frac{-\mathbb{A}_X}{2} + \frac{2}{M_x N_x} + \frac{16}{M_x N_x} \sum_l \frac{l}{\pi \alpha_x} A_{x_3}^{-1}$$

$$\times \left({}_1F_1\left(1, \frac{3}{2}, \frac{1}{A_{x_3}\alpha_x}\right) + {}_1F_1\left(1, \frac{3}{2}, \frac{4l^2}{A_{x_3}\alpha_x}\right) \right)$$

$$- 2 \frac{A_{x_2}}{\pi \alpha_x} \beta_4^{-1} \left({}_1F_1\left(1, \frac{3}{2}, \frac{A_{x_1}^2}{\beta_4 \alpha_x}\right) + {}_1F_1\left(1, \frac{3}{2}, \frac{1}{\beta_4 \alpha_x}\right) \right)$$

$$+ \frac{k_x}{\pi \alpha_x} \beta_5^{-1} {}_1F_1\left(1, \frac{3}{2}, \frac{1}{\beta_5 \alpha_x}\right) \right) + A_3 \left(\alpha^\nu \left(\frac{\Gamma(\mu+\nu)}{\mu} \right. \right.$$

$$\times \left(\frac{\mathbb{A}_X \mathbb{F}_2(\mu, \alpha, \beta_1)}{2\sqrt{\pi \alpha_x}} - \frac{A_{x_2}}{\sqrt{\pi \alpha_x}} \mathbb{F}_2(\mu, \alpha, \beta_2) \right) + \sum_n$$

$$\times \frac{\Gamma(\mu_2+\nu)}{\mu_2} \left(\frac{-16}{M_x N_x} \sum_l \frac{l}{\pi \alpha_x} \mathbb{F}_2(\mu_2, \alpha, \beta_3) \left(\left(\frac{1}{\alpha_x} \right)^n \right. \right.$$

$$+ \left(\frac{4l^2}{\alpha_x} \right)^n \right) - 2 \frac{A_{x_2}}{\pi \alpha_x} \mathbb{F}_2(\mu_2, \alpha, \beta_4) \left(\left(\frac{1}{\alpha_x} \right)^n \right.$$

$$+ \left(\frac{A_{x_1}^2}{\alpha_x} \right)^n \right) - \frac{k_x}{\pi \alpha_x} \mathbb{F}_2(\mu_2, \alpha, \beta_5) \left(\frac{1}{\alpha_x} \right)^n \right) \right) \Bigg),$$

(37)

where $\nu = \frac{1}{2} + k_1$; $\alpha = \frac{1}{2\bar{\gamma}_u \sigma_{\gamma_u}^2}$, $\mu_1 = n + \frac{1}{2}$, $\beta_1 = \frac{1}{\alpha_x} + \Omega$, and $\beta_2 = \frac{A_{x_1}^2}{\alpha_x} + \Omega$. Further, $\mu_2 = n + i + 1$, $\beta_3 = A_{x_3} + \Omega$, $\beta_4 = \frac{1 + A_{x_1}^2}{\alpha_x} + \Omega$, and $\beta_5 = \frac{2}{\alpha_x} + \Omega$.

Ergodic rate analysis

The ergodic rate for system model SM-2 can be obtained by substituting the e2e SNR of SM-2 in (23).

Lemma 7. The generalized ergodic rate expressio of the system model 1(b) is given as

$$C_{R_2} = \frac{A_3}{2\ln 2} \sum_{j=0}^{\infty} \frac{(-\Omega)^j}{j!} \frac{1^{n+j}}{\Gamma(1)} G_{1+1,2+1}^{2+1,0+1} \left(\beta \left| \begin{matrix} 1-\rho, a_1, ..., a_p \\ \sigma - \rho, b_1, ..., b_q \end{matrix} \right. \right)$$

(38)

where

$$A_3 = e^{-\alpha_2^2/2} \sum_{k_2=0}^{\infty} \sum_{l=0}^{\infty} \sum_{n=0}^{l} \frac{K_i^l \Omega_i^n}{(l)! n!} \frac{1}{k_2!} \left(\frac{\alpha_2^2}{2} \right)^{k_2} \frac{\exp[-K]}{\Gamma(M_2 + k_2)}.$$

Further, $\rho = n + j + 1$, $\beta_1 = 1$, $\sigma = 1$, $\alpha = \beta$, $m = 2, n = 0, p = 1$, and $q = 2$.

Proof:
Proof is given in Appendix G ∎

VI. Numerical Analysis

In this section, the numerical results are presented and the accuracy of the analytical expressions is evaluated with the Monte-Carlo simulations. Unless otherwise stated, the considered simulation parameters are given in TABLE 4. In figures, 'Ana', Asym., and 'Sim', indicate the 'analytical', 'asymptotic' and 'simulation results', respectively. Further

'SM-1' and 'SM-2' indicate the considered System Model 1 and System Model 2 (as shown in Figure 1(a) and Figure 1(b)), respectively. In figures, Analytical results are represented by solid lines whereas the simulation results are represented by markers.
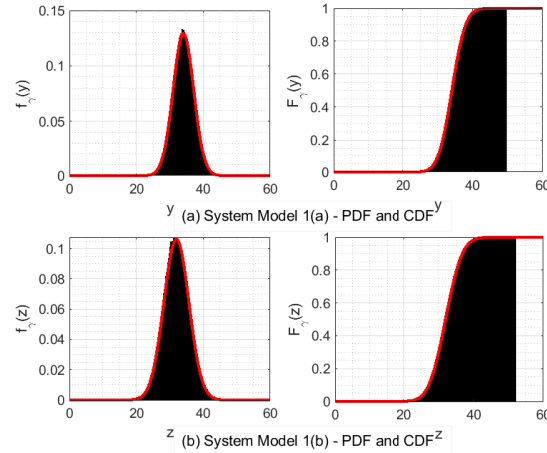

FIGURE 2. PDFs and CDFs of IRS links of system models 1, 2 (as shown in Figure 1(a) and Figure 1(b)).

In Figure 2, the PDFs and CDFs correspond to the IRS links of system models 1 and 2, respectively are presented to verify the central limit theorem (CLT). In Figure 2(a), CLT is verified through the histogram plot for both PDF and CDF correspond to $S \rightarrow H_I \rightarrow U$ link with Rician and SR fading. In Figure 2(b), CLT is verified through the histogram plot for both PDF and CDF corresponding to $H_R \rightarrow I \rightarrow U$ link with SR and Nakagami-m fading.

The OP curves are presented in Figure 3 for both system models under HS fading with 30 IRS elements. In Figure 3(a), for SM-1, HAP gain is considered to be IRS elements gain whereas in SM-2, HAP gain of 30 dB is considered. The overall system performance of SM-2 is dominated by the $S \rightarrow H_R$ link performance than the $H_R \rightarrow I \rightarrow U$ link. Thus, the system with the aerial assisted IRS node (SM-1) outperforms the system with the terrestrial assisted IRS node (SM-2). In Figure 3(b), SM-1 OP results are compared with SM-2 OP results for various HAP gains. To ensure a fair comparison, we consider 30 IRS elements and set K to 5 in the SM-1 scenario. IRS elements gain constitutes the HAP gain for SM-1. Results illustrate that with the increase in HAP gain from 30 dB to 105 dBm [46], OP performance of SM-2 improves over the SM-1 OP performance. Finally, simulation results match well with the analytical results.

Results in Figure 4, demonstrate the impact of IRS elements and the Rician parameter over the OP of the SM-1. In Figure 4(a), OP versus transmit power is presented for SM-1 for different IRS elements. For an OP of 10^{-8}, system with 150 IRS elements provides a transmit power gain of ≈ 35 dBm and ≈ 4 dBm as compared to the system with 30 and 120 IRS elements, respectively. The increase in transmit power gain reduces with the increase in IRS elements. In

TABLE 3. Functional representation in Arithmetic expressions

Function	Representation
A_3	$e^{-\alpha_2^2/2} \sum\limits_{k_2=0}^{\infty} \sum\limits_{l=0}^{\infty} \sum\limits_{n=0}^{l} \dfrac{K_i^l \Omega_i^n}{(l)! n!} \dfrac{1}{k_2!} \left(\dfrac{\alpha_2^2}{2}\right)^{k_2} \dfrac{\exp[-K]}{\Gamma(M_2+k_2)}$
$\sum\limits_{y=0}$; $\mathbb{F}_2(a_1, b_1, c_1)$	$\sum\limits_{y=0}^{\infty} \dfrac{(1)_y}{(\frac{3}{2})_y y!}$; $\dfrac{1}{(b_1+c_1)^{a_1+\vartheta}} {}_2F_1\left(1, a_1+\vartheta, a_1+1, \dfrac{c_1}{b_1+c_1}\right).$

TABLE 4. Simulation Parameters

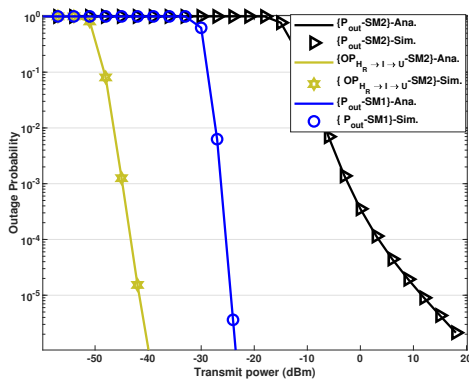| Parameters	System model 1	System model 2
Carrier frequency f_c	5 GHz	5 GHz
Light velocity c	3×10^8 m/s	3×10^8 m/s
Height of satellite	$35,786$ Km	$35,786$ Km
Height of HAP	20 Km	20 Km
G_{Max}	56 dBi	56 dBi
$\{\phi_{\text{SH}}, \phi_{\text{3dB}}\}$	$\{0.4°, 0.8°\}$	$\{0.4°, 0.8°\}$
G_H	N_{IRS}	105 dB [46], [47]
user gain	$G_{Rx} = 2$	$Gr_U = 2$
L_{Rain}	0.01 dB/Km	0.01 dB/Km
$L_{\text{Atm.}}$	5.4×10^{-3} dB/Km	5.4×10^{-3} dB/Km
L_{oth}	2 dB	2 dB
$\{h_t, h_r\}$	-	$\{50, 5\}$ m
$d_{\text{I}_N\text{U}}$		300m
Heavy shadowing (HS)	$b_0 = 0.063\ m_0 = 1\ \Omega_0 = 0.0007$	$b_0 = 0.063\ m_0 = 1\ \Omega_0 = 0.0007$
Average shadowing (AS)	$b_0 = 0.251\ m_0 = 5\ \Omega_0 = 0.279$	$b_0 = 0.251\ m_0 = 5\ \Omega_0 = 0.279$
Light shadowing (LS)	$b_0 = 0.158\ m_0 = 19\ \Omega_0 = 1.29$	$b_0 = 0.158\ m_0 = 19\ \Omega_0 = 1.29$

Figure 4(b), OP performance of SM-1 is presented with respect to the transmit power for different Rician fading paramters and shadowing effects. For an OP of 10^{-8}, system with K=3 has a transmit power gain of 0.75 dBm and ≈ 1.2 dBm over $K = 6$ and $K = 9$, respectively (irrespective to the shadowing conditions). Further, for an OP of 10^{-8}, LS has a transmit power gain of ≈ 12 dBm and ≈ 14 dBm over AS and HS conditions.

Ergodic rate analysis is shown in Figure 5 and illustrated the effect of fading conditions and the IRS elements for SM-1 with $K = 5$. In Figure 5(a), the curves depicts the affect of IRS elements under LS over ergodic rate. With an increase in IRS elements from 30 to 960, the ergodic rate increases from 15 bps/Hz to 25 bps/Hz. With every two-folds increase in IRS elements, the ergodic rate increases by ≈ 2 bps/Hz. The effects of shadowing are shown in Figure 5(b). For 30 dBm transmit power, system under LS has ergodic rate gain of ≈ 1.93 bps/Hz over the system under HS. Finally, the derived simulation results matches closely with the analytical results.
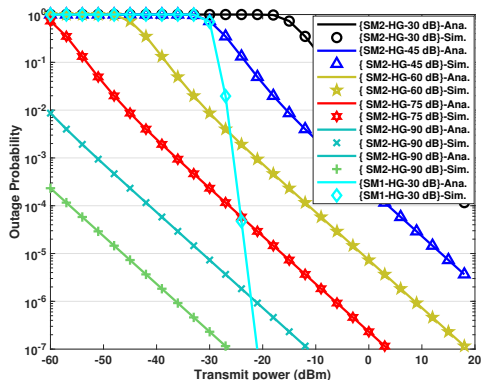
In Figure 6, ergodic rate analysis of the SM-2 is presented with respect to the transmit power under LS. The comparison between the ergodic rates of SM-1 and SM-2 are depicted in Figure 6(a). For SM-1, 30 IRS elements are considered, while SM-2 utilizes a HAP gain of 105 dBm. The results highlight that the overall ergodic rate achieved in SM-2 is dominated by the S $\rightarrow$ H$_R$ link, exhibiting a rate of 4.17 bps/Hz, surpassing the ergodic rate of 44.59 bps/Hz for the H$_R$ $\rightarrow$ I $\rightarrow$ U link at 30 dBm transmit power. Thus, the aerial IRS node based SM-1 outperforms the terrestrial IRS node based SM-2 with a ergodic rate of ≈ 15 bps/Hz. In Figure 6(b), ergodic rates of SM-2 are presented for Rician parameters $K = \{1, 3, 6\}$ for a HAP gain of 105 dBm. Additionally, ergodic rates for $K = 6$ with HAP gains $105, 75, 30$ dBm are shown to realize the effects of both K parameters and HAP gain on the ergodic rates. The results indicate that, for a transmit power of 30 dBm and a HAP gain of 105 dBm, the system with $K = 6$ achieves an ergodic rate gain of 0.15 bps/Hz over the system with $K = 1$. This marginal improvement signifies the changes in the HAP gain have limited impact on the overall performance. For $K = 6$, the system with a HAP gain of 105 dBm has an ergodic rate gain of ≈ 0.0025 bps/Hz over a system with a HAP gain of 30 dBm. This observation is attributed to the fact that the overall diversity gain of SM-2 is dominated by the diversity gain of the S $\rightarrow$ H$_R$ link, while in SM-1, the ergodic rates attained are directly proportional to the diversity gain of IRS elements.

ASER results for various QAM schemes are demonstrated in Figure 7 for SM-1 under HS scenario for $K = 3$. In Figure 7(a) ASER analysis of SQAM, RQAM, and XQAM are shown whereas in Figure 7(b) HQAM results are plotted

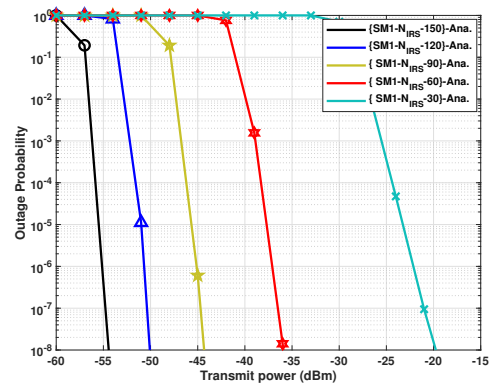(a) OP vs transmit power of SM-1 and SM-2 for 30 IRS elements.
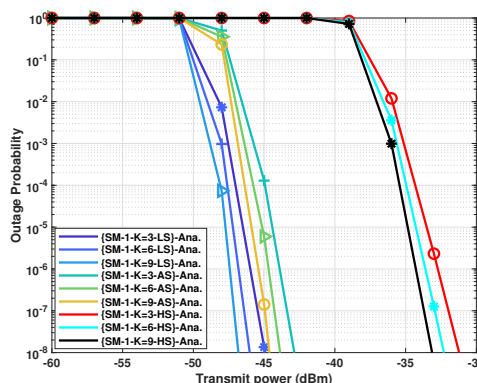

(a) OP performance of SM-1 for various IRS elements.
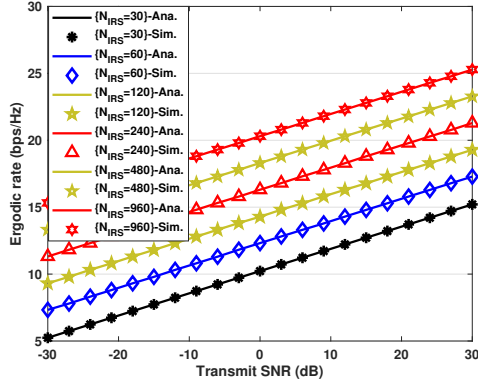

(b) OP vs transmit power of SM-1 and SM-2 for various HAP gains.

(b) OP performance of SM-1 for various various Rician parameters under different shadowing conditions.

FIGURE 3. Outage probability versus transmit power of SM-1 and SM-2.

FIGURE 4. Impact of IRS elements and the Rician factor over OP performance of SM-1.

for constellation points 4, 8, 16, 32, and 64. Monte-Carlo simulations closely align with the derived analytical results, demonstrating good agreement. For an ASER of 10^{-2}, 32-XQAM has a transmit power gain of ≈ 2 dBm over 8×4 RQAM.

In Figure 8, even and odd higher order constellations ASER results are shown for various QAM schemes under AS scenario with 30 IRS elements and $K = 3$. In Figure 8(a), the even constellation points 64, 256, and 1024 are presented. The results clearly demonstrate that as the constellation sizes increase from 64, 256, and 1024, HQAM outperforms the SQAM with a transmit power gain of ≈ 1 dBm. This improvement is attributed to the optimum 2 dimensional hexagonal lattice of HQAM with minimum peak and average power than the SQAM. In Figure 8(b), the ASER analysis of RQAM, XQAM, and HQAM is presented with odd constellation points (32, 128, and 512). It is observed that for odd bits transmission also, HQAM outperforms both RQAM and XQAM. For an ASER of 10^{-4}, 32 HQAM has transmit power gain of ≈ 0.25 dBm over the XQAM and ≈ 2 dBm over 8×4 RQAM. Additionally, for an ASER of 10^{-2}, HQAM has transmit power gain of ≈ 0.2 dBm for 128 and 512 constellations sizes, respectively. These findings

indicates the superiority of HQAM in achieving improved performance across different constellation sizes.

In Figure 9, comparative ASER analysis results for various QAM schemes between SM-1 and SM-2 with 30 IRS elements under HS scenario are presented. In Figure 9(a), ASER analysis of HQAM for both SM-1 and SM-2 is presented for constellation points 4, 8, 16, 32, and 64. For an ASER of 10^{-1}, for all the constellation points, SM-1 consistently exhibits an average transmit power gain of ≈ 18 dBm over SM-2. The overall system performance in SM-1 is significantly boosted with the IRS elements. On the other hand, in SM-2, the system's performance is influenced by the S $\rightarrow$ H$_R$ link, impacting its overall efficiency. In Figure 9(b), ASER analysis of HQAM, SQAM, RQAM, and XQAM is represented for 16 and 32 constellation points for both SM-1 and SM-2. For an ASER of 10^{-3}, 16-HQAM has a transmit power gain of ≈ 0.85 dBm over 16-SQAM, while for 32- constellation points, HQAM achieves a gain of ≈ 0.3 dBm and ≈ 1.5 dBm over the XQAM and RQAM schemes, respectively. For SM-2, an ASER of 10^{-1}, 16-HQAM exhibits a transmit power gain of ≈ 0.6 dBm over the 16-SQAM. The performance gain of HQAM over other
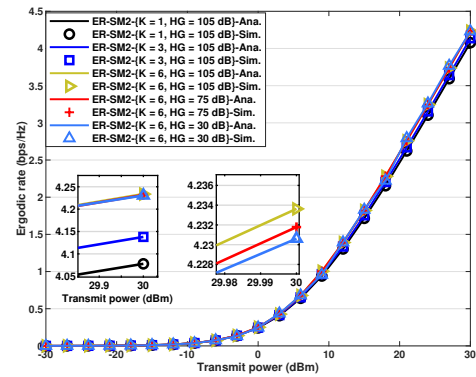
(a) Impact of IRS elements.

(b) Impact of shadowing.

FIGURE 5. Ergodic rate versus transmit power of SM-1.
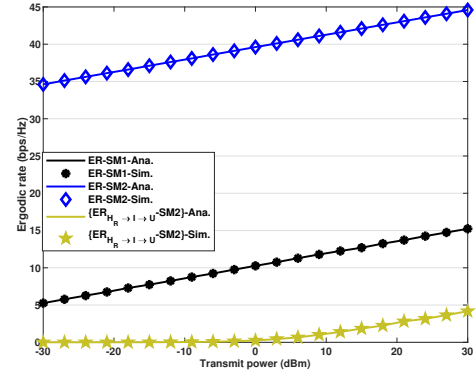
(a) Ergodic rate of SM-1 and SM-2 for 30 IRS elements.
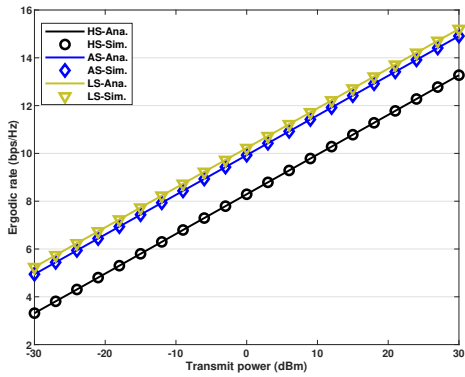
(b) Ergodic rate of SM-2 for various Rician parameters values and HAP gains.

FIGURE 6. Ergodic rate versus transmit power.

QAM schemes is due to its low peak and average energies with optimum 2 dimensional hexagonal constellation.

VII. Conclusion

In this study, performance analysis of satellite-terrestrial networks with aerial and terrestrial IRS nodes over diverse fading channels, including shadowed Rician, Rician, and Nakagami-m fading channels is presented. System performance is examined through the closed-form expressions of outage probability, ergodic rate, and average symbol error rate for the higher-order modulation schemes. Practical antenna gains, path losses, and various link fading scenarios are taken into account to characterize the satellite-terrestrial links accurately. The analysis reveals that SM-1, operating under heavy shadowing conditions, outperforms SM-2, which operates under lighter shadowing. Aerial IRS node based system exhibits superior performance compared to the terrestrial IRS node based system. The overall ergodic rate attained in an aerial IRS node system is proportional to the IRS elements, whereas in the terrestrial IRS node-based system, the overall ergodic rate is influenced by the diversity provided by the satellite-HAP link. By considering more HAP gain in SM-2, the overall system performance can be enhanced compared to SM-1. Additionally, in SM-1, a notable observation is that

with every increase in IRS elements by two-folds, the ergodic rate increases by ≈ 2 bps/Hz whereas for SM-2, ergodic rate is dominated by ergodic rate of the S $\rightarrow$ H$_R$ link. It is also observed that for both even and odd bits transmission, HQAM outperforms the other QAM schemes.

Appendix A
Proof of Lemma 1

Proof:

In (13), it is observed that γ is the sum of products of α_i and β_i which are independent Rician and shadowed Rician fading channels, respectively. To facilitate the mathematical tractability the PDF and cumulative distribution function (CDF) of γ are approximated tightly.

Statistical characterization of the optimal received SNR
By invoking central limit theorem (CLT), in (13), the PDF and CDF of γ are approximated with $R = \bar{\gamma}Z^2$, where in $Z = \sum_{i=0}^{N} \tilde{Z}$ Let $\tilde{Z} = XY$ where X and Y are independent
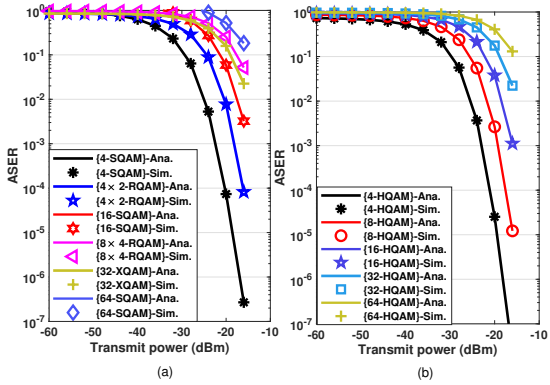
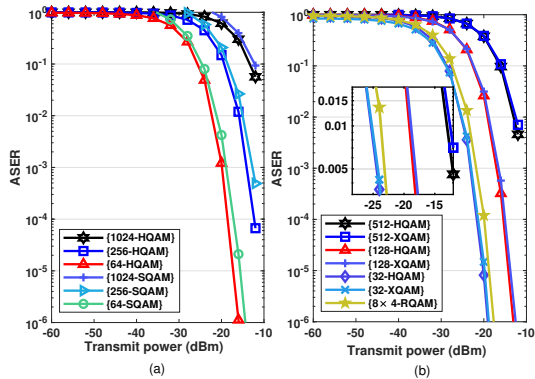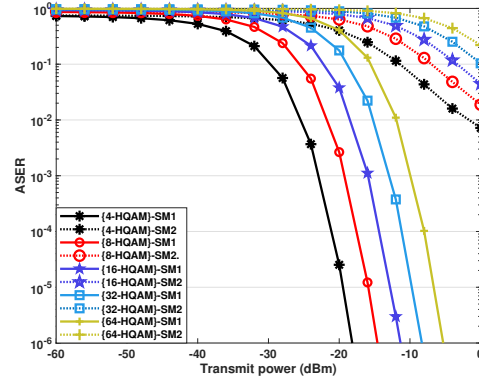**FIGURE 7.** ASER vs transmit power of SM-1 for various constellations.

FIGURE 8. ASER vs transmit power of SM-1 for higher order constellation sizes.

(a) ASER analysis of HQAM for SM-1 and SM-2.

(b) ASER analysis of 16 and 32 constellation points

FIGURE 9. ASER analysis of various modulation schemes.

random variables. Mean and variance of $\tilde{Z}$ are given as:
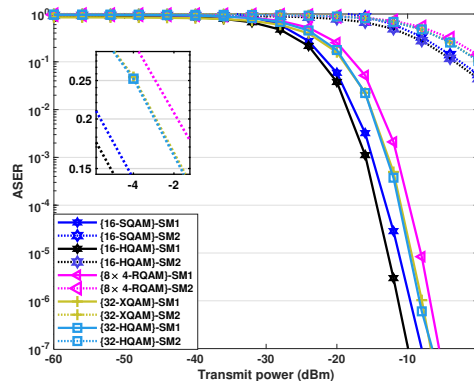
$$
\mathrm{E}(\tilde{Z}) = \left(4\sigma_R^2 b_0\right)^{1/2} \Gamma\left(\frac{3}{2}\right) B_0^m {}_1F_1\left(-\frac{1}{2}, 1; -K\right)
$$
$$
\times\, {}_2F_1\left(\frac{3}{2},\, m,\, 1,\, B_1\right), \tag{39}
$$

$$
\mathrm{Var}(\tilde{Z}) = \frac{2(2b_0)\bar{\gamma}_i^2}{(1+K)^2} B_0^m {}_1F_1\left(-2, 1; -K\right) {}_2F_1\left(2,\, m,\, 1,\, B_1\right)
$$
$$
-\frac{(2b_0)^{1/2}\bar{\gamma}_i}{(1+K)} \Gamma\left(\frac{3}{2}\right) B_0^m {}_1F_1\left(-1, 1; -K\right)
$$
$$
\times\, {}_2F_1\left(\frac{3}{2},\, m,\, 1,\, B_1\right), \tag{40}
$$

where $B_0 = \left(\frac{2b_0 m_h}{2b_0 m_h + \Omega}\right)$ and $B_1 = \frac{\Omega}{2b_0 m_h + \Omega}$. Mean and variance of Z are given as $\mu_Z = \mathrm{E}[Z] = \sum_{i=1}^{N} \mathrm{E}[\tilde{Z}_i]$ and $\sigma_Z^2 = \mathrm{Var}[Z] = \sum_{i=1}^{N} \mathrm{Var}[\tilde{Z}_i]$, respectively. In practice, the meta-surface IRS elements are of conformal geometry, light weight, low cost, and size. Hence, it is practically possible to use large number of reflecting surfaces. Thus, for sufficiently large number of reflecting meta-surfaces, and as per CLT Z^2 follows a non-central chi-square random variable with one degree of freedom with mean $\mu_Z = N\mu_{\tilde{Z}}$ and variance $\sigma_Z^2 = N\sigma_{\tilde{Z}}^2$.

The PDF of γ is given as

$$
f_\gamma(\gamma) = \frac{1}{2\sigma_\gamma^2 \bar{\gamma}} \left(\frac{\gamma}{\bar{\gamma}\mu_\gamma^2}\right)^{-\frac{1}{4}} \exp\left(-\frac{\gamma + \mu_\gamma^2 \bar{\gamma}}{2\bar{\gamma}\sigma_\gamma^2}\right)
$$
$$
\times I_{-\frac{1}{2}}\left(\frac{\mu_\gamma \sqrt{\gamma}}{\sqrt{\bar{\gamma}}\sigma_\gamma^2}\right), \quad \gamma > 0 \tag{41}
$$

where $\mu_\gamma = \mu_Z$ and $\sigma_\gamma = \sigma_Z$. The CDF is given as [38, eq. (2.3-35)]

$$
F_\gamma(\gamma) = 1 - Q_{\frac{1}{2}}\left(\frac{\mu_\gamma}{\sigma_\gamma}, \frac{\sqrt{\gamma}}{\sqrt{\bar{\gamma}}\sigma_\gamma}\right), \quad \gamma > 0 \tag{42}
$$

∎

Appendix B
Proof of Lemma 2

Proof:

To derive the closed-form ASER expression for HQAM, the first order derivative of the conditional SEP (17) is obtained by using the identities $Q(x) = \frac{1}{2}\left[1 - \mathrm{erf}\left(\frac{x}{\sqrt{2}}\right)\right]$ and [48, Eq. (7.1.21)] and differentiating it w.r.t γ as

To derive the closed-form ASER expression for HQAM, the (15) can be rewritten by taking the approximation of

:

Marcum-Q function as given in [44, eq. 18] as

$$F_{\gamma_{e2e}}(\gamma) = 1 - \sum_{k_1=0}^{\infty} e^{-\alpha_1^2/2} \frac{1}{k_1!} \left(\frac{\alpha_1^2}{2}\right)^{k_1} \frac{\Gamma(\frac{1}{2}+k_1, B_{\gamma_u}\gamma)}{\Gamma(\frac{1}{2}+k_1)}.$$

(43)

where $B_{\gamma_u} = \left(\frac{1}{2\bar{\gamma}_u \sigma_{\gamma_u}^2}\right)$. On substituting $P_s'(e|\gamma)$ and $F_{\gamma_{e2e}}(\gamma)$, respectively into (16), we get

$$P_s{}^H = -\int_0^{\infty} P_s'(e|\gamma) F_{\gamma_{e2e}}(\gamma) d\gamma,$$
$$= -\int_0^{\infty} P_s'(e|\gamma) d\gamma + A_2 \int_0^{\infty} P_s'(e|\gamma)$$
$$\times \Gamma\left(\frac{1}{2}+k_1, B_{\gamma_u}\gamma\right) d\gamma = -P_{H_1} + P_{H_2}, \quad (44)$$

P_{H_1} can be resolved by using the identities [45, eq. 3.351.3, eq. 7.522.9] and is given as

$$P_{H_1} = \frac{-H_a}{2} + \frac{2H_b}{3} + \frac{H_b}{3\pi} {}_2F_1\left(1,1,\frac{3}{2},\frac{1}{2}\right) + \frac{3H_b}{4\sqrt{3}\pi}$$
$$\times \left({}_2F_1\left(1,1,\frac{3}{2},\frac{1}{2}\right) + {}_2F_1\left(1,1,\frac{3}{2},\frac{1}{4}\right)\right). \quad (45)$$

P_{H_2} can be resolved by using

$$P_{H_2} = A_2 \int_0^{\infty} P_s'(e|\gamma) \Gamma\left(\frac{1}{2}+k_1, B_{\gamma_u}\gamma\right) d\gamma,$$
$$= A_2 \int_0^{\infty} \left(\frac{1}{2}\sqrt{\frac{\alpha_h}{2\pi}}(H_b - H_a)\gamma^{-\frac{1}{2}} e^{-\frac{\alpha_h\gamma}{2}} - \frac{H_b}{3}\sqrt{\frac{\alpha_h}{3\pi}}\right.$$
$$\times \gamma^{-\frac{1}{2}} e^{-\frac{\alpha_h\gamma}{3}} + \frac{H_b}{2}\sqrt{\frac{\alpha_h}{6\pi}}\gamma^{-\frac{1}{2}} e^{-\frac{\alpha_h\gamma}{6}}\right)$$
$$\times \Gamma\left(\frac{1}{2}+k_1, B_{\gamma_u}\gamma\right) d\gamma + A_2 \int_0^{\infty} \left(\frac{2H_b\alpha_h}{9\pi} e^{-\frac{2\alpha_h\gamma}{3}}\right.$$
$$\times {}_1F_1\left(1,\frac{3}{2},\frac{\alpha_h}{3}\gamma\right) - \frac{H_b\alpha_h}{2\sqrt{3}\pi} e^{-\frac{2\alpha_h\gamma}{3}}$$
$$\times \left\{{}_1F_1\left(1,\frac{3}{2},\frac{\alpha_h}{2}\gamma\right) + {}_1F_1\left(1,\frac{3}{2},\frac{\alpha_h}{6}\gamma\right)\right\}\right)$$
$$\times \Gamma\left(\frac{1}{2}+k_1, B_{\gamma_u}\gamma\right) d\gamma. \quad (46)$$

The above expression can be resolved by using the identity [45, eq. 6.455.1, eq.9.14.1], and given as:

$$P_{H_2} = A_2\left(\alpha^{\nu}\left(\frac{\Gamma(\mu+\nu)}{\mu}\left(\frac{1}{2}\sqrt{\frac{\alpha_h}{2\pi}}(H_b - H_a)\mathbb{F}_2(\mu,\alpha,\beta_1)\right.\right.\right.$$
$$- \frac{H_b}{3}\sqrt{\frac{\alpha_h}{3\pi}}\mathbb{F}_2(\mu,\alpha,\beta_2)\frac{H_b}{2}\sqrt{\frac{\alpha_h}{6\pi}}\mathbb{F}_2(\mu,\alpha,\beta_3)\right) + \sum_n$$
$$\times \frac{\Gamma(\mu_2+\nu)}{\mu_2}\mathbb{F}_2(\mu_2,\alpha,\beta_4)\left(\frac{2H_b\alpha_h}{9\pi}\left(\frac{\alpha_h}{3}\right)^n - \frac{H_b\alpha_h}{2\sqrt{3}\pi}\right.$$
$$\times \left.\left.\left.\left\{\left(\frac{\alpha_h}{2}\right)^n + \left(\frac{\alpha_h}{6}\right)^n\right\}\right)\right)\right). \quad (47)$$

On substituting (45) and (47) in (44), to get the closed-form expression as given in (18). ∎

Appendix C
Proof of Lemma 3

Proof:

ASER expression for the RQAM scheme is also derived by using the CDF approach. The first order derivative of conditional SEP of RQAM scheme is derived by following the similar approach as in Appendix (B).

Further, substituting $P_s'(e|\gamma)$ and $F_{\gamma_{e2e}}(\gamma)$, respectively into (16), we get

$$P_s{}^R = -\int_0^{\infty} P_R'(e|\gamma) F_{\gamma_{e2e}}(\gamma) d\gamma,$$
$$= -\int_0^{\infty} P_R'(e|\gamma) d\gamma + A_2 \int_0^{\infty} P_R'(e|\gamma)$$
$$\times \Gamma\left(\frac{1}{2}+k_1, B_{\gamma_u}\gamma\right) d\gamma, = -P_{R_1} + P_{R_2}, \quad (48)$$

P_{R_1} can be resolved by using the identities [45, eq. 3.351.3, eq. 7.522.9] as

$$P_{R_1} = a_r R_1(R_2 - 1) + b_r R_2(R_1 - 1) - \frac{a_r b_r R_1 R_2}{\pi}\beta_3^{-1}$$
$$\times \left\{{}_1F_1\left(1,\frac{3}{2},\frac{B_r}{\beta_3}\right) + {}_1F_1\left(1,1,\frac{3}{2},\frac{A_r}{\beta_3}\right)\right\}. \quad (49)$$

Similarly, P_{R_2} is resolved by using the identities [45, eq. 9.14.1, eq. 6.455.1] as

$$P_{R_2} = A_2\left(\alpha^{\nu}\left(\frac{\Gamma(\mu+\nu)}{\mu}\left(\frac{a_r R_1(R_2 - 1)}{\sqrt{2\pi}}\mathbb{F}_2(\mu,\alpha,\beta_1)\right.\right.\right.$$
$$\times + \frac{b_r R_2(R_1 - 1)}{\sqrt{2\pi}}\mathbb{F}_2(\mu,\alpha,\beta_2)\right) - \sum_n \frac{a_r b_r R_1 R_2}{\pi}$$
$$\times \left.\left.\frac{\Gamma(\mu_2+\nu)}{\mu_2}\mathbb{F}_2(\mu_2,\alpha,\beta_3)\left(B_r^n + A_r^n\right)\right)\right). \quad (50)$$

On substituting (49) and (50) in (48) to get the generalized ASER expression for RQAM as given in (20). ∎

Appendix D
Proof of Lemma 4

Proof:

First order derivative of conditional SEP expression (51) for XQAM is derived by following the similar approach as in Appendix (B) and using the identity [45, (9.14.1)] and is given as

$$P_X'(e|\gamma) = \left(\frac{\mathbb{A}_X}{2\sqrt{\pi\alpha_x}}e^{-\frac{\gamma}{\alpha_x}} - \frac{A_{x_2}}{\sqrt{\pi\alpha_x}}e^{-\frac{A_{x_1}^2\gamma}{\alpha_x}}\right)\gamma^{\frac{-1}{2}} + \sum_n \gamma^n$$
$$\times \left\{\frac{-16}{M_x N_x}\sum_l\left\{\frac{l}{\pi\alpha_x}e^{-\gamma A_{x_3}}\left(\left(\frac{1}{\alpha_x}\right)^n + \left(\frac{4l^2}{\alpha_x}\right)^n\right)\right\}\right.$$
$$- \frac{2A_{x_2}}{\pi\alpha_x}e^{-\gamma\frac{(1+A_{x_1}^2)}{\alpha_x}}\left(\left(\frac{1}{\alpha_x}\right)^n + \left(\frac{A_{x_1}^2}{\alpha_x}\right)^n\right) - \frac{k_x}{\pi\alpha_x}$$
$$\times \left.e^{\frac{-2\gamma}{\alpha_x}}\left(\frac{1}{\alpha_x}\right)^n\right\}. \quad (51)$$

IEEE Open Journal of the
Communications Society

where $\mathbb{A}_X = \left(-A_n + k_x + \frac{4}{M_x N_x} \left(2 \sum_{l=1}^{\frac{A_{x_1}}{2} - 1} + 1 \right) \right)$. The generalized closed-form ASER expression of XQAM can be obtained by substituting $P'_s(e|\gamma)$ and $F_{\gamma_{e2e}}(\gamma)$ from (51) and (43), respectively in (16) and is given as

$$
\begin{aligned}
P_s{}^X &= -\int_0^\infty P'_X(e|\gamma) F_{\gamma_{e2e}}(\gamma) d\gamma, \\
&= -\int_0^\infty P'_X(e|\gamma) d\gamma + A_2 \int_0^\infty P'_X(e|\gamma) \\
&\quad \times \Gamma\left(\frac{1}{2} + k_1, B_{\gamma_u}\gamma\right) d\gamma \\
&= -P_{X_1} + P_{X_2},
\end{aligned}
\tag{52}
$$

$P_{X_1} = \int_0^\infty P'_X(e|\gamma) d\gamma$ can be resolved by using the identity [45, eq. 3.351.3] as

$$
\begin{aligned}
P_{X_1} &= \frac{-1}{2}\mathbb{A}_X + \frac{2}{M_x N_x} + \frac{16}{M_x N_x} \sum_l \frac{l}{\pi \alpha_x} A_{x_3}^{-1} \\
&\quad \times \left({}_1F_1\left(1, \frac{3}{2}, \frac{1}{A_{x_3}\alpha_x}\right) + {}_1F_1\left(1, \frac{3}{2}, \frac{4l^2}{A_{x_3}\alpha_x}\right) \right) \\
&\quad - 2\frac{A_{x_2}}{\pi\alpha_x}\beta_4^{-1}\left({}_1F_1\left(1, \frac{3}{2}, \frac{A_{x_1}^2}{\beta_4\alpha_x}\right) + {}_1F_1\left(1, \frac{3}{2}, \frac{1}{\beta_4\alpha_x}\right) \right) \\
&\quad + \frac{k_x}{\pi\alpha_x}\beta_5^{-1} {}_1F_1\left(1, \frac{3}{2}, \frac{1}{\beta_5\alpha_x}\right) \Bigg).
\end{aligned}
\tag{53}
$$

P_{X_2} can be obtained by using the identity [45, eq. 6.455.1] as

$$
\begin{aligned}
P_{X_2} &= A_2 \Bigg(\alpha^\nu \Bigg(\frac{\Gamma(\mu+\nu)}{\mu} \left(\frac{\mathbb{A}_X}{2\sqrt{\pi\alpha_x}} \mathbb{F}_2(\mu,\alpha,\beta_1) - \frac{A_{x_2}}{\sqrt{\pi\alpha_x}} \right. \\
&\quad \times \mathbb{F}_2(\mu,\alpha,\beta_2) \Bigg) + \sum_n \frac{\Gamma(\mu_2+\nu)}{\mu_2}\left(\frac{-16}{M_x N_x} \sum_l \frac{l}{\pi\alpha_x} \right. \\
&\quad \times \mathbb{F}_2(\mu_2,\alpha,\beta_3)\left(\left(\frac{1}{\alpha_x}\right)^n + \left(\frac{4l^2}{\alpha_x}\right)^n \right) - 2\frac{A_{x_2}}{\pi\alpha_x} \\
&\quad \times \left(\left(\frac{1}{\alpha_x}\right)^n + \left(\frac{A_{x_1}^2}{\alpha_x}\right)^n \right) \mathbb{F}_2(\mu_2,\alpha,\beta_4) - \frac{k_x}{\pi\alpha_x} \\
&\quad \times \mathbb{F}_2(\mu_2,\alpha,\beta_5)\left(\frac{1}{\alpha_x}\right)^n \Bigg) \Bigg) \Bigg).
\end{aligned}
\tag{54}
$$

On substituting (53) and (54) in (52), the generalized ASER expression for XQAM is obtained as in (22). ∎

Appendix E
Proof of Lemma 5

Proof:

On substituting (43) in (23), the integral is given as

$$
\begin{aligned}
C_R &= \frac{1}{2\ln 2}\int_0^\infty \frac{1 - \left(1 - A_2\Gamma\left(\frac{1}{2}+k_1, B_{\gamma_u}\gamma\right)\right)}{1+\gamma} d\gamma \\
&= \frac{A_2}{2\ln 2}\int_0^\infty \frac{\Gamma\left(\frac{1}{2}+k_1, B_{\gamma_u}\gamma\right)}{1+\gamma} d\gamma.
\end{aligned}
\tag{55}
$$

The exact analysis of the above integral is not possible and hence the $\Gamma(a,b)$ can be represented in terms of Meijer-G

function by using the identity given in [49, eq. 8.4.16.2]. (55) can be re-written as

$$
C_{R_2} = \frac{A_2}{2\ln 2}\int_0^\infty \frac{G_{1,2}^{2,0}1}{1+\gamma}\left(\beta\gamma \left| \begin{matrix} 1 \\ 0, \alpha \end{matrix} \right.\right) d\gamma,
\tag{56}
$$

where $\beta = \frac{1}{2\bar\gamma\sigma_\gamma^2}$ and $\alpha = \frac{1}{2} + k_1$. The above integral can be resolved by using the identity [45, eq. 7.8.11.5] to get the closed-form ergodic rate expression for $S \to H_I \to U$ link as in (23) ∎

Appendix F
Proof of Lemma 6

Proof:

The closed-form outage probability expression can be obtained by derived the CDFs corresponding to γ_s and γ_u. γ_s, is the instantaneous SNR corresponds to the $S \to R$ link which is Rician fading channel. The CDF of γ_s is given as [38, eq. 2.3-57]

$$
F_{\gamma_s}(\gamma_{th}) = 1 - Q_1\left(\frac{\mu_{\gamma_s}}{\sigma_{\gamma_s}}, \frac{\gamma_{th}}{\sigma_{\gamma_s}}\right), \quad \gamma_{th} > 0
\tag{57}
$$

$\sigma_{\gamma_s} = \sqrt{\frac{\mu_{\gamma_s}^2}{2K}}$ [38, eq. 2.3-60]. In (30), γ_u is the sum of products of λ_i and κ_i which are independent shadowed Rician and Nakagami-m fading channels, respectively. A similar approach is followed to characterize the PDF and CDF of γ_u as in Appendix A. Lets consider $\gamma_u = \bar\gamma_u A^2$, where in $A = \sum_{i=0}^N \tilde{A}$ Let $\tilde{A} = BC$ where B and C are independent random variables. The mean and variances of $\tilde{A}$ are given as $\mu_A = \mathrm{E}(A) = \sum_{i=1}^N \mathrm{E}(\tilde{A}_i) = N\mathrm{E}(\tilde{A})$ and $\sigma_A^2 = \mathrm{Var}(A) = \sum_{i=1}^N \mathrm{Var}(\tilde{A}_i) = N\mathrm{Var}(\tilde{A})$, respectively. Wherein

$$
\begin{aligned}
\mathrm{E}(\tilde{A}) &= \frac{\Gamma(m_g + \frac{1}{2})}{\Gamma(m_g)}\left(\frac{\sigma_g^2}{m_g}\right)^{\frac{1}{2}} B_0^{m_h}(2b_0)^{1/2}\Gamma\left(\frac{3}{2}\right) \\
&\quad \times {}_2F_1\left(\frac{3}{2}, m_h, 1, B_1\right),
\end{aligned}
\tag{58}
$$

$$
\begin{aligned}
\mathrm{Var}(\tilde{A}) &= \frac{\Gamma(m_g + 1)}{\Gamma(m_g)}\left(\frac{\sigma_g^2}{m_g}\right) B_0^{m_h}(2b_0){}_2F_1\left(2, m_h, 1, B_1\right) \\
&\quad - \left(\frac{\Gamma(m_g + \frac{1}{2})}{\Gamma(m_g)}\left(\frac{\sigma_g^2}{m_g}\right)^{\frac{1}{2}} B_0^{m_h}(2b_0)^{1/2}\Gamma\left(\frac{3}{2}\right) \right. \\
&\quad \left. \times {}_2F_1\left(\frac{3}{2}, m_h, 1, B_1\right)\right)^2.
\end{aligned}
\tag{59}
$$

Thus, by invoking CLT for sufficiently large number of reflecting meta-surfaces A^2 follows a non-central chi-square random variable with one degree of freedom with mean $\mu_A = N\mu_{\tilde{A}}$ and variance $\sigma_A^2 = N\sigma_{\tilde{A}}^2$. Hence, the CDF of γ_{su} is given by [38, eq. (2.3-35)]

$$
F_{\gamma_u}(\gamma_u) = 1 - Q_{\frac{1}{2}}\left(\frac{\mu_{\gamma_u}}{\sigma_{\gamma_u}}, \frac{\sqrt{\gamma_u}}{\sqrt{\bar\gamma_u}\sigma_{\gamma_u}}\right), \quad \gamma_u > 0
\tag{60}
$$

where $\mu_{\gamma_u} = \mu_A$ and $\sigma_{\gamma_u} = \sigma_A$. On substituting (57) and (60) in (32), to get the closed-form expression as given in (33). ∎

:

Appendix G
Proof of Lemma 7

Proof:

On substituting (34) in (23), the integral is given as

$$C_R = \frac{1}{2\ln 2} \int_0^\infty \frac{1 - \left(1 - A_3 \exp[-\Omega\gamma]\Gamma(\tfrac{1}{2} + k_2, \beta_2^2/2)\gamma^n\right)}{1+\gamma} d\gamma,$$

$$= \frac{A_3}{2\ln 2} \int_0^\infty \gamma^n \exp[-\Omega\gamma] \frac{\Gamma(\tfrac{1}{2} + k_1, B_{\gamma_u}\gamma)}{1+\gamma} d\gamma, \quad (61)$$

By using the identities [49, eq. 8.4.16.2] and [45, eq. 1.211.1], (61), can be re-written as

$$C_{R_2} = \frac{A_3}{2\ln 2} \sum_{j=0}^\infty \frac{(-\Omega)^j}{j!} \int_0^\infty \gamma^{n+j}(1+\gamma)^{-1} G_{1,2}^{2,0}\left(\beta\gamma \middle| \begin{matrix} 1 \\ 0, \alpha \end{matrix}\right) d\gamma,$$

$$(62)$$

The above integral is resolved by using the identity [45, eq. 7.811.5] to get the closed expression for ergodic rate of the system model Figure 1(b) as given in (38). ∎

References

[1] A. Chaoub, M. Giordani, B. Lall, V. Bhatia, A. Kliks, L. Mendes, K. Rabie, H. Saarnisaari, A. Singhal, N. Zhang *et al.*, "6G for bridging the digital divide: Wireless connectivity to remote areas," *IEEE Wireless Commun.*, vol. 29, no. 1, pp. 160–168, Jul. 2021.

[2] M. Giordani and M. Zorzi, "Non-terrestrial networks in the 6G era: Challenges and opportunities," *IEEE Netw.*, vol. 35, no. 2, pp. 244–251, Dec. 2020.

[3] Q. Huang, M. Lin, W.-P. Zhu, S. Chatzinotas, and M.-S. Alouini, "Performance analysis of integrated satellite-terrestrial multiantenna relay networks with multiuser scheduling," *IEEE Trans. Aerospace Electron. Sys.*, vol. 56, no. 4, pp. 2718–2731, Nov. 2019.

[4] ETSI TR 138 912 V15.0.0 , "Study on New Radio (NR) to support non-terrestrial networks," 2020.

[5] W. U. Khan, A. Mahmood, C. K. Sheemar, E. Lagunas, S. Chatzinotas, and B. Ottersten, "Reconfigurable Intelligent Surfaces for 6G Non-Terrestrial Networks: Assisting Connectivity from the Sky," *arXiv preprint arXiv:2309.02859*, 2023.

[6] J. Liu, Y. Shi, Z. M. Fadlullah, and N. Kato, "Space-air-ground integrated network: A survey," *IEEE Commun. Surv. Tuts.*, vol. 20, no. 4, pp. 2714–2741, May. 2018.

[7] C. L. Holloway, E. F. Kuester, J. A. Gordon, J. O'Hara, J. Booth, and D. R. Smith, "An overview of the theory and applications of metasurfaces: The two-dimensional equivalents of metamaterials," *IEEE Antennas Propag. Mag.*, vol. 54, no. 2, pp. 10–35, Apr. 2012.

[8] R. Alghamdi, R. Alhadrami, D. Alhothali, H. Almorad, A. Faisal, S. Helal, R. Shalabi, R. Asfour, N. Hammad, A. Shams *et al.*, "Intelligent surfaces for 6G wireless networks: A survey of optimization and performance analysis techniques," *IEEE Access*, Oct. 2020.

[9] K. Tekbıyık, G. K. Kurt, A. R. Ekti, A. Görçin, and H. Yanikomeroglu, "Reconfigurable intelligent surfaces empowered THz communication in LEO satellite networks," *arXiv preprint arXiv:2007.04281*, Jul. 2020.

[10] S. Xu, J. Liu, Y. Cao, J. Li, and Y. Zhang, "Intelligent reflecting surface enabled secure cooperative transmission for satellite-terrestrial integrated networks," *IEEE Trans. Veh. Technol.*, vol. 70, no. 2, pp. 2007–2011, Feb. 2021.

[11] J. Li, S. Xu, J. Liu, Y. Cao, and W. Gao, "Reconfigurable intelligent surface enhanced secure aerial-ground communication," *IEEE Trans. Commun.*, vol. 69, no. 9, pp. 6185–6197, Jun. 2021.

[12] Z. Lin, M. Lin, B. Champagne, W.-P. Zhu, and N. Al-Dhahir, "Secrecy-energy efficient hybrid beamforming for satellite-terrestrial integrated networks," *IEEE Trans. Commun.*, vol. 69, no. 9, pp. 6345–6360, Jun. 2021.

[13] Z. Lin, H. Niu, K. An, Y. Wang, G. Zheng, S. Chatzinotas, and Y. Hu, "Refracting RIS-aided hybrid satellite-terrestrial relay networks: Joint beamforming design and optimization," *IEEE Trans. Aerospace Electron. Sys.*, vol. 58, no. 4, pp. 3717–3724, Mar. 2022.

[14] Z. Lin, H. Niu, K. An, Y. Hu, D. Li, J. Wang, and N. Al-Dhahir, "Pain without gain: Destructive beamforming from a malicious RIS perspective in IoT networks," *IEEE Internet Things J.*, 2023.

[15] H. Ibrahim, H. Tabassum, and U. T. Nguyen, "Exact coverage analysis of intelligent reflecting surfaces with Nakagami-m channels," *IEEE Trans. Veh. Technol.*, vol. 70, no. 1, pp. 1072–1076, Jan. 2021.

[16] B. Zhao, M. Lin, M. Cheng, J.-B. Wang, J. Cheng, and M.-S. Alouini, "Robust Downlink Transmission Design in IRS-Assisted Cognitive Satellite and Terrestrial Networks," *IEEE J. Sel. Areas Commun.*, Jun. 2023.

[17] S. Alfattani, W. Jaafar, Y. Hmamouche, H. Yanikomeroglu, A. Yongaçoglu, N. D. Dào, and P. Zhu, "Aerial platforms with reconfigurable smart surfaces for 5G and beyond," *IEEE Commun. Mag.*, vol. 59, no. 1, pp. 96–102, Feb. 2021.

[18] K. Tekbiyik, G. Kurt, A. Ekti, and H. Yanikomeroglu, "Reconfigurable Intelligent Surfaces in Action: For Nonterrestrial Networks: Employing Reconfigurable Intelligent Surfaces," *IEEE Veh. Technol. Mag.*, 2022.

[19] E. Björnson, Ö. Özdogan, and E. G. Larsson, "Intelligent reflecting surface versus decode-and-forward: How large surfaces are needed to beat relaying?" *IEEE Wireless Commun. Lett.*, vol. 9, no. 2, pp. 244–248, Oct. 2019.

[20] M. Di Renzo, K. Ntontin, J. Song, F. H. Danufane, X. Qian, F. Lazarakis, J. De Rosny, D.-T. Phan-Huy, O. Simeone, R. Zhang *et al.*, "Reconfigurable intelligent surfaces vs. relaying: Differences, similarities, and performance comparison," *IEEE Open J. Commun. Soc.*, vol. 1, pp. 798–807, Jun. 2020.

[21] K. Dolas and M. R. Bhatnagar, "On Performance of IRS-Assisted Hybrid Satellite-Terrestrial Cooperative Communication," *IEEE Trans. Aerospace Electron. Sys.*, Aug. 2022.

[22] H. Dong, C. Hua, L. Liu, W. Xu, and R. Tafazolli, "Intelligent Reflecting Surface-Aided Integrated Terrestrial-Satellite Networks," *IEEE Trans. Wireless Commun.*, Oct. 2022.

[23] Q. Tao, J. Wang, and C. Zhong, "Performance analysis of intelligent reflecting surface aided communication systems," *IEEE Commun. Lett.*, vol. 24, no. 11, pp. 2464–2468, 2020.

[24] A. Mahmoud, S. Muhaidat, P. C. Sofotasios, I. Abualhaol, O. A. Dobre, and H. Yanikomeroglu, "Intelligent reflecting surfaces assisted UAV communications for IoT networks: Performance analysis," *IEEE Trans. Green Commun. Netw.*, vol. 5, no. 3, pp. 1029–1040, Mar. 2021.

[25] P. K. Singya, P. Shaik, N. Kumar, V. Bhatia, and M.-S. Alouini, "A Survey on Higher-Order QAM Constellations: Technical Challenges, Recent Advances, and Future Trends," *IEEE Open J. Commun. Soc.*, vol. 2, pp. 617–655, Mar. 2021.

[26] S. Parvez, P. K. Singya, and V. Bhatia, "On ASER analysis of energy efficient modulation schemes for a device-to-device MIMO relay network," *IEEE Access*, vol. 8, pp. 2499–2512, Dec. 2019.

[27] S. Parvez, P. K. Singya, and V. Bhatia, "On impact of imperfect CSI over hexagonal QAM for TAS/MRC-MIMO cooperative relay network," *IEEE Commun. Lett.*, vol. 23, no. 10, pp. 1721–1724, Jul. 2019.

[28] P. Shaik, P. K. Singya, and V. Bhatia, "Performance analysis of QAM schemes for non-regenerative cooperative MIMO network with transmit antenna selection," *AEU-Int. J. Electron. Commun.*, vol. 107, pp. 298–306, Jul. 2019.

[29] P. K. Singya and M.-S. Alouini, "Performance of UAV assisted Multiuser Terrestrial-Satellite Communication System over Mixed FSO/RF Channels," *IEEE Trans. Aeros. Electron. Syst.*, Sep. 2021.

[30] K. K. Garg, P. Shaik, V. Bhatia, and O. Krejcar, "On the performance of a relay assisted hybrid RF-NLOS UVC system with imperfect channel estimation," *J. Optical Commun. Netw.*, vol. 14, no. 4, pp. 177–189, 2022.

[31] E. Cianca, R. Prasad, M. De Sanctis, A. De Luise, M. Antonini, D. Teotino, and M. Ruggieri, "Integrated satellite-HAP systems," *IEEE Commun. Mag.*, vol. 43, no. 12, pp. supl–33, Dec. 2005.

[32] G. Karabulut Kurt, M. G. Khoshkholgh, S. Alfattani, A. Ibrahim, T. S. J. Darwish, M. S. Alam, H. Yanikomeroglu, and A. Yongacoglu, "A Vision and Framework for the High Altitude Platform Station (HAPS) Networks of the Future," *IEEE Commun. Surv. Tutor.*, vol. 23, no. 2, pp. 729–779, 2021.

[33] O. B. Yahia, E. Erdogan, and G. K. Kurt, "HAPS-assisted hybrid RF-FSO multicast communications: Error and outage analysis," *IEEE Trans. Aerospace Electron. Sys.*, vol. 59, no. 1, pp. 140–152, Jun. 2022.

[34] X. Li, Y. Li, X. Song, L. Shao, and H. Li, "RIS assisted UAV for weather-dependent satellite terrestrial integrated network with hybrid FSO/RF systems," *IEEE Photonics Journal*, 2023.

[35] D. Singh, R. Swaminathan, and A. T. Pham, "Multiple HAPS-based space-air-ground network with FSO communication: a performance analysis," *Applied Optics*, vol. 63, no. 9, pp. 2362–2375, 2024.

[36] A. Abdi, W. C. Lau, M.-S. Alouini, and M. Kaveh, "A new simple model for land mobile satellite channels: First-and second-order statistics," *IEEE Trans. Wireless Commun.*, vol. 2, no. 3, pp. 519–528, May 2003.

[37] H. A. Suraweera, G. K. Karagiannidis, and P. J. Smith, "Performance analysis of the dual-hop asymmetric fading channel," *IEEE Trans. Wireless Commun.*, vol. 8, no. 6, pp. 2783–2788, Jun.

[38] J. G. Proakis and M. Salehi, "Digital Communications, McGraw-Hill," *Inc., New York,*, 1995.

[39] H. Shuai, K. Guo, K. An, Y. Huang, and S. Zhu, "Transmit Antenna Selection in NOMA-based Integrated Satellite-HAP-Terrestrial Networks with Imperfect CSI and SIC," *IEEE Wireless Commun. Lett.*, Apr. 2022.

[40] E. Basar, M. Di Renzo, J. De Rosny, M. Debbah, M.-S. Alouini, and R. Zhang, "Wireless communications through reconfigurable intelligent surfaces," *IEEE Access*, vol. 7, pp. 116 753–116 773, Aug. 2019.

[41] K. Garg, P. Shaik, V. Bhatia, and O. Krejcar, "On the performance of relay assisted hybrid RF-NLOS UVC sy.stem with imperfect channel estimation," *J. Optical Commun. Netw.*, vol. 14, no. 3, Dec. 2021.

[42] S. Parvez, P. K. Singya, V. Bhatia, and N. Kumar, "ASER Analysis of Cross QAM for TAS/MRC-MIMO Cooperative Relay System with Imperfect CSI," in *IEEE Adv. Net. Telecommun. Syst. (ANTS)*. IEEE, 2019, pp. 1–7.

[43] D. Sadhwani and R. N. Yadav, "A simplified exact expression of SEP for cross QAM in AWGN channel from M×N rectangular QAM and its usefulness in Nakagami-m fading channel," *AEU - International Journal of Electronics and Communications*, vol. 74, pp. 63 – 74, 2017.

[44] A. Annamalai, C. Tellambura, and J. Matyjas, "A new twist on the generalized Marcum Q-function QM (a, b) with fractional-order M and its applications," in *IEEE Consumer Commun. Netw. Conf.* IEEE, Jan. 2009, pp. 1–5.

[45] I. S. Gradshteyn and I. M. Ryzhik, *Table of integrals, series, and products*. Academic Press, 2014.

[46] 3GPP, "Universal Terrestrial Radio Access (UTRA): repeater planning guidelines and system analysis," *3rd Generation Partnership Project (3GPP), TR 25.956 V16.0.0*, Jun. 2020.

[47] Y. Xing, F. Hsieh, A. Ghosh, and T. S. Rappaport, "High altitude platform stations (HAPS): Architecture and system performance," in *IEEE Veh. Technol. Conf.* IEEE, Apr. 2021, pp. 1–6.

[48] M. Abramowitz and I. A. Stegun, *Handbook of mathematical functions: with formulas, graphs, and mathematical tables*. 9th ed. New York, NY, USA: Dover, 1970.

[49] A. P. Prudnikov, J. A. Bryčkov, and O. I. Maričev, *Integrals and series. vol. 3, More special functions*. New York: Gordon and Breach, 1989.

Shaik Parvez earned his Ph.D. in Electrical Engineering from the Indian Institute of Technology Indore, India. Following his doctorate, he served as a research associate at IIT Indore and a visiting postdoctoral fellow at IISc Bangalore. Presently, he holds a postdoctoral research associate position with Texas A&M University at QATAR. Dr. Parvez is a peer reviewer for several top-tier journals, including TVT, TCOM, IEEE CL, and System Journal, among others. He acted as a co-chair for IEEE ANTS 2022. His research focuses on various aspects of communication networks, such as MIMO cooperative networks, terrestrial and non-terrestrial communications, RF and optical communications (including NOn-LOS UVC and VLC), IRS, and deep learning.

Kamal K. Garg received his M.Tech. degree in signal processing from the Netaji Subhash Institute of Technology (currently NSUT), New Delhi, India, in 2002, and completed his Ph.D. from the Indian Institute of Technology Indore, India, in 2022. He presently serves as a Faculty member at Pandit Deendayal Energy University, Gandhinagar, India. With over 15 years of experience in the field of satellite mobile communications, he has contributed significantly to this industry. His research interests encompass signal processing, as well as the design and performance analysis of RF and optical wireless communication systems. He is an esteemed Reviewer for prominent academic journals and conferences, including IEEE, OSA, and Optica.

Vimal Bhatia (Senior Member, IEEE) received the Ph.D. degree from the Institute for Digital Communications, The University of Edinburgh, Edinburgh, U.K., in 2005. He is currently a Professor with the Indian Institute of Technology (IIT) Indore, India, and an Adjunct Faculty Member of IIT Delhi and IIIT Delhi, India. During the Ph.D. degree, he also received the IEE Fellowship for collaborative research with the Department of Systems and Computer Engineering, Carleton University, Canada. He is also a Young Faculty Research Fellow from MeitY, Government of India. He was a recipient of the Prof SVC Aiya Memorial Award, in 2019. He has worked with various IT companies for over 11 years, both in India and the U.K. He is also a PI/Co-PI/Coordinator for external projects with funding of over USD 20 million from MeitY, DST, UKIERI, MoE, AKA, IUSSTF, and KPMG. His research interests include communications, non-Gaussian nonparametric signal processing, and machine/deep learning with applications to communications and photonics. He is a fellow of IETE and OSI and a certified SCRUM Master. He has served as the Founder and the Head for the Center for Innovation and Entrepreneurship, the Associate Dean of Research and Development, and the Dean of Academic Affairs. He is also a DRISHTI CPS Chair Professor with IIT Indore. He has been mentioned among the world's top 2% scientists by Stanford University.

Ondrej Krejcar received the Ph.D. degree in technical cybernetics from the Technical University of Ostrava, Czech Republic, in 2008. He is currently a Full Professor in systems engineering and informatics at the University of Hradec Kralove (UHK), Czech Republic. He is currently the Vice-Dean for science and research at the Faculty of Informatics and Management, UHK. He is also the Director of the Center for Basic and Applied Research, University of Hradec Kralove, Czech Republic. His research interests include control systems, smart sensors, ubiquitous computing, wireless technology, biomedicine, image segmentation and recognition, biometrics, cybernetics, ubiquitous computing, biotelemetric system architecture (portable device architecture and wireless biosensors), and development of applications for mobile devices with use of remote or embedded biomedical sensors

Mohamed-Slim Alouini (Fellow, IEEE) received the Ph.D. degree in electrical engineering from the California Institute of Technology (Caltech), Pasadena, CA, USA, in 1998. He served as a faculty member at the University of Minnesota, Minneapolis, MN, USA, then at Texas A & M University at Qatar, Education City, Doha, Qatar before joining King Abdullah University of Science and Technology (KAUST), Thuwal, Makkah Province, Saudi Arabia as a professor of electrical engineering in 2009. His current research interests include the modeling, design, and performance analysis of wireless communication systems